
2 Atomic Force Acoustic Microscopy

Ute Rabe

Abbreviations

a_1, a_2, a_3, a_4 and A_1, A_2, A_3, A_4	Constants in the shape function $y(x)$
a_C	Contact radius
α	Wave number of the flexural waves
A	Cross-section area of the cantilever
b	Thickness of the cantilever
c_P	Ratio ϕ_{Lat}/ϕ
d_{Y0}, d_{X0}	Normalized amplitude of the sensor tip in y - and x -direction, respectively
δ_n, δ_L	Normal, lateral contact deflection (in the coordinate system of the sample surface)
E	Young's modulus of the cantilever
E^*	Reduced Young's modulus of the contact
ε	Displacement of the additional mass m_L from the center of the beam
E_T, E_S	Young's modulus of the tip, the surface
G^*	Reduced shear modulus of the contact
G_T, G_S	Shear modulus of the tip, the surface
F_n, F_L	Normal, lateral forces (in the coordinate system of the sample surface)
f	Frequency
φ	Tilt angle of the cantilever
ϕ, ϕ_{Lat}	Dimensionless normal, lateral contact function
Φ	Phase
γ, γ_{Lat}	Normal, lateral contact damping
h	Height of the sensor tip
η_{Air}	Damping constant describing losses by air
I	Area moment of inertia
L	Length of the cantilever
L_1	Distance from the fixed end of the cantilever to the position of the tip
L_2	Distance from the free end of the beam to the tip
k^*, k_{Lat}^*	Normal, lateral contact stiffness
k_C	Static spring constant of the cantilever

m^*, m	Effective mass, real mass of the cantilever
m_L	Additional mass
M	Moment
M_T, M_S	Indentation modulus of the tip, the sample surface
$N(\alpha), N_0(\alpha)$	Denominators in the formulas for forced vibration of the beam
p, p_{Lat}	Dimensionless normal, lateral contact damping
Q	Quality factor
R	Radius of the sensor tip
ρ	Mass density of the cantilever
S	Contact area
S_0, S_1, S_2, S_3, S_4	Terms in the characteristic equation
σ	Sensitivity
t	Time
u_0	Amplitude of excitation
w	Width of the cantilever
x, x_2	Coordinate in length direction of the cantilever
y, y_2	Deflection of the cantilever in its thickness direction
X, T, U	Auxiliary functions in the boundary conditions
ω	Circular frequency
Ω	Characteristic function
ψ	$\psi = \alpha L$ dimensionless wave number
AFAM	Atomic force acoustic microscopy
AFM	Atomic force microscopy
FMM	Force modulation microscopy
SAFM	Scanning acoustic force microscopy
SAM	Scanning acoustic microscopy
SLAM	Scanning local acceleration microscopy
SMM	Scanning microdeformation microscopy
UAFM	Ultrasonic atomic force microscopy
UFM	Ultrasonic force microscopy

2.1

Introduction

Materials with an artificial nanostructure such as nanocrystalline metals and ceramics or matrix embedded nanowires or nanoparticles are advancing into application. Polymer blends or piezoelectric ceramics are examples for materials of high technical importance possessing a natural nanostructure which determines their macroscopic behavior. Structures such as thin films or adhesion layers are of nm dimensions in only one direction, but micromechanical devices and even nano-devices are feasible which are of nm size in three dimensions. In the nm range the mechanical properties such as hardness or elastic constants and the symmetry of the crystal lattice can vary with the size of the object. Furthermore, the properties of structures with nm-dimensions depend strongly on the surrounding material and on the boundary conditions in general. Therefore there is a need to measure mechanical properties on a nano-scale.

2.1.1

Near-field Acoustic Microscopy

Ultrasonic imaging based on transmission and reflection of ultrasonic waves has been used for a long time for elasticity measurements and flaw detection in different areas such as physics, nondestructive testing and medicine. By measuring the dispersion of laser generated surface acoustic waves in the frequency range of several 10 MHz up to several 100 MHz, the elastic constants of thin films can be determined [1]. The distance covered by the acoustic wave between the generating laser spot and the receiver (about 10 mm) defines the lateral resolution of this technique. In the classical scanning acoustic microscopy (SAM), which was developed in the 1970th, an acoustic wave is focused onto the sample surface by a sapphire lens, and the reflected acoustic waves are detected [2]. The imaging contrast depends on the acoustic impedance ρv (ρ = mass density of the sample, v = sound velocity) and consequently on the elastic constants of the sample. Defects like cracks, inclusions or mechanical stresses influence the acoustic impedance and can also be imaged if they are in a certain penetration depth inside the sample.

According to Abbe's principle, techniques using focused waves are restricted in their lateral resolution to about half a wavelength. A focused acoustic beam in water yields a spot diameter of about 1 μm at 1 GHz frequency. The local resolution can be improved if an acoustic wave is guided towards the sample by a structure which is smaller and closer to the surface than the acoustic wavelength. Different acoustic microscopes based on this near-field principle were proposed [3–6]. One drawback of this type of microscope is a low signal level because the traveling acoustic waves have to pass through an nm-scaled structure. Alternatively, the near-field sensor can be constituted by a small object which vibrates at one of its resonant frequencies. G  thner et al. used a resonating tuning fork [7] vibrating at 33 kHz in air. One corner of the tuning fork served as a sensor tip. Hydrodynamic interaction between the sensor tip and the sample surface damps the vibration and shifts the resonant frequency of the tuning fork. As the damping depends mainly on the thickness of the air layer between sensor and sample, there is almost no contrast by the elasticity of the sample, but the technique can be used to image topography. More recently, tuning forks or length extension quartz resonators are used as force sensors for high-resolution atomic force microscopy in air and in vacuum [8].

After the invention of the Atomic Force Microscope (AFM) [9] near field microscopy was strongly promoted and various operation modes and related techniques emerged. Since 1993, several microscopes combining AFM with ultrasonic imaging have been developed, named for example ultrasonic force microscopy (UFM) [10], scanning acoustic force microscopy (SAFM) [11], atomic force acoustic microscopy (AFAM) [12], and ultrasonic atomic force microscopy (UAFM) [13]. These techniques can be considered as special types of dynamic force microscopy or as near-field techniques from the point of view of ultrasonic imaging. The sensor tip of the AFM has a radius of only several nm up to several 100 nm. The tip-sample contact radius, which is orders of magnitude smaller than the acoustic wavelength, defines the local resolution.

To reach high local resolution, nanoscaled probes can either be used as emitters or as detectors of ultrasound. In the latter case acoustic waves are generated with

conventional ultrasonic transducers, and a scanning probe microscope is used to detect the acoustic wave fields at the sample surface. In atomic force microscopy the tip-sample forces are a nonlinear function of tip-sample distance. The nonlinear forces cause frequency mixing, if an ultrasonic excitation signal is applied to a transducer below the sample and another vibration with a slightly different frequency is excited in the cantilever and its sensor tip [11, 14]. In the scanning acoustic force microscopy [14] mixing of two surface waves which propagate in different direction is exploited to image surface acoustic wave fields with submicron lateral resolution. Interference phenomena caused by scattering of a plane wave by a disk-shaped structure were observed in this way [15].

The nonlinearity of the tip-sample forces has a rectifying effect which is exploited in ultrasonic force microscopy [10, 16]. In UFM, an ultrasonic transducer generating longitudinal waves is placed below the sample. The amplitude of the sinusoidal excitation applied to the transducer is modulated with a saw-tooth signal. The acoustic wave causes a high frequency out-of-plane surface vibration with a low-frequency amplitude modulation. The sensor tip of the AFM is in contact with the vibrating sample surface and when the threshold amplitude is reached, the sensor tip lifts off from the surface. A lock-in amplifier which operates at the modulation frequency detects the envelope of the high frequency signal. This rectifying property was called “mechanical diode effect”. A qualitative image of elastic sample properties and contrast from subsurface objects can be obtained [16–18]. A rectifying effect due to the nonlinear forces is also observed when the amplitude modulated vibration is excited at the fixed end of the cantilever (“waveguide UFM”) [19]. The contrast in UFM was examined by different research groups [20, 21]. The advantage of the mixing technique and the UFM is the low bandwidth which is required for the position detector in the AFM. Because the modulation frequency can be chosen in the kHz range, a direct detection of signals at MHz or even GHz frequencies is not necessary. As both, elasticity and adhesion, contribute to the image contrast [22], it is difficult to separate surface elasticity quantitatively from adhesion.

2.1.2

Scanning Probe Techniques and Nanoindentation

Different dynamic operation modes of the scanning force microscope were suggested to measure elasticity on an nm scale. In the force-modulation mode (FMM) the sensor tip is in contact with the probed surface, and the surface is vibrated normally or laterally at a frequency below the first resonance of the cantilever [23]. The amplitude or phase of the vibration of the cantilever is evaluated. Force modulation microscopy provides elasticity contrast of softer samples like for example polymers. If stiffer materials like metals and ceramics are to be examined, the contact stiffness between tip and surface becomes much higher than the spring constant of the cantilever (0.1 N/m up to several 10 N/m, depending on the type of beam) and the contrast decreases. Instead of applying the force indirectly by varying the distance between the surface and the fixed end of the cantilever, other research groups applied a magnetic force directly to the cantilever [24, 25]. Some authors extend force-modulation microscopy to the higher modes of the cantilever [25–27]. Here, this type of operation is called contact-resonance spectroscopy and will be treated in detail in the next paragraphs.

In the pulsed force mode [28] the distance between the fixed end of the sensor and the sample surface is also modulated at a frequency below the resonant frequencies of the sensor. The amplitude is so high (10–500 nm) that the tip loses contact with the sample surface during its vibration cycle. Characteristic points in the vibration signal of the cantilever are evaluated to image elasticity and adhesion. In scanning local acceleration microscopy (SLAM) the sensor tip is in contact with a sample surface that is vibrated out-of-plane with a frequency slightly above the first flexural resonance of the cantilever [29]. Using a temperature controlled SLAM instrument, Oulevey et al. observed martensitic phase transformation in NiTi-alloy [30].

Force-modulation microscopy can be considered as direct detection of low frequency acoustical vibrations by an AFM. A sensor tip which touches the sample surface during its vibration cycle for example in FMM or tapping mode [31] radiates sound into the sample, but the amplitudes are usually below the detection limit of commercial transducers [32]. If the sensor of the AFM is magnified by only one or two orders of magnitude like in scanning microdeformation microscopy (SMM), the acoustical amplitudes transmitted through the sample become detectable [33]. Subsurface features were imaged by SMM in transmission mode [34]. The vibration of the cantilever was measured with a piezoelectric element [35] or with an optical interferometer pointing onto the cantilever [36]. The AFM sensor and the SMM cantilever are so similar to each other that many aspects of the equation of motion and the contact mechanics models are identical. As the radius of the SMM sensor tip is larger than the radius of an AFM tip the tip-sample interaction is easier to control and macroscopic contact models are easier to apply. Because the contact area scales with the size of the sensor tip, the lateral resolution is lower in SMM than in the AFM based techniques.

Nanoindentation, which was originally developed to measure hardness, can also be used for elasticity measurements [37]. In dynamic nanoindentation a low amplitude sinusoidal force modulation is superimposed to the quasi static load applied to the indenter. Amplitude and phase of the vibration of the electromechanical system, constituted by the indenter and the force detection unit, are evaluated to measure contact stiffness as a function of load [38]. The indenter tips are of Berkovich type made of diamond or spherical with a radius of 100 μm . The local resolution of the nanoindenter is typically 100 nm to 200 nm because of the mechanical stress field in the sample at a minimum penetration depth of about 20 nm. Seyed Asif et al. imaged the real and imaginary parts of the Young's modulus of carbon fibers in epoxy matrix by dynamic nanoindentation [39]. Especially for examination of softer materials like polymers, dynamic nanoindentation became very popular during the last years. An overview of commercial instruments can be found for example in a publication by Bushan and Li [40].

2.1.3

Vibration Modes of AFM Cantilevers

The typical dimensions of cantilevers for atomic force microscopy are several 100 μm in length, several 10 μm in width and several 100 nm up to several μm in thickness. The sensors are small plates or beams having distributed mass, and they can be excited to different modes of vibration such as flexural or torsional modes. While

most of the dynamic scanning probe applications relied on the fundamental modes of the beams, for noise analysis the importance of the higher eigenmodes was recognized by different authors [41, 42]. In atomic force acoustic microscopy and ultrasonic atomic force microscopy the flexural resonant frequencies of atomic force microscope cantilevers are measured [13, 43, 44]. The sensor of the AFM can be considered as a cantilever beam which is clamped at one end and free at the other end. If the sensor tip is in contact with a sample surface tip-sample interaction forces change the end conditions and all resonant frequencies of the cantilever are shifted. Furthermore, tip-sample interaction causes damping and changes the width of the resonance curves.

When the cantilever is in flexural vibration, a large component of the amplitude of the tip apex is normal to the sample surface. Therefore flexural modes are used to measure normal tip-sample contact stiffness, which in turn depends on the Young's modulus of tip and sample, on the shear modulus of tip and sample, on the contact area, and on the adhesion forces. In most cases, the flexural modes cause an angular oscillation of the cantilever beam at the position where the tip is fixed, which in turn leads to an oscillation of the tip apex parallel to the surface. This means that the flexural modes are also influenced by lateral tip-sample contact stiffness and friction.

Torsion of AFM cantilevers is used to measure lateral forces and friction [45, 46] and a variety of dynamic operation modes exploiting torsional vibration is known. Similar to AFAM and UAFM the torsional resonant frequency and the width of the resonant peaks can be determined to measure in-plane surface properties [47, 48]. At low amplitudes the sensor tip sticks to the sample surface, and at higher amplitudes sliding sets in. The stick-slip events cause a characteristic plateau in the shape of the contact-resonance curves [49]. Torsional modes are not the only type of vibration exhibiting a strong component of lateral tip-sample amplitude. Bending of the cantilever in its thickness direction leads to non-negligible lateral tip-sample displacement [50], and lateral bending modes of the cantilever can be used for imaging and spectroscopy [51]. In the so-called "overtone atomic force microscopy" Drobeck et al. exploited the torsional vibration modes of V-shaped cantilevers to measure in-plane surface stiffness [52, 53]. Elasticity contrast was obtained on Al-Ni-Fe quasicrystal samples [52], and the lateral stiffness of Si, Al, and CdTe surfaces was evaluated quantitatively [53]. The results were obtained in ambient conditions by analysis of the thermal noise of the cantilevers.

2.2

Linear Contact-resonance Spectroscopy Using Flexural Modes

Contact-resonance spectroscopy techniques which exploit the flexural modes of the cantilevers can be organized according to the method of excitation. In the AFAM-technique a transducer below the sample excites longitudinal waves which cause out-of-plane vibrations of the investigated surface (transducer 1 in Fig. 2.1) [43, 44]. Via the tip-sample contact forces the vibrations are transmitted into the cantilever. The flexural vibrations can also be excited by a transducer which generates oscillations of the fixed end of the beam (transducer 2 in Fig. 2.1). This technique (UAFM) was first

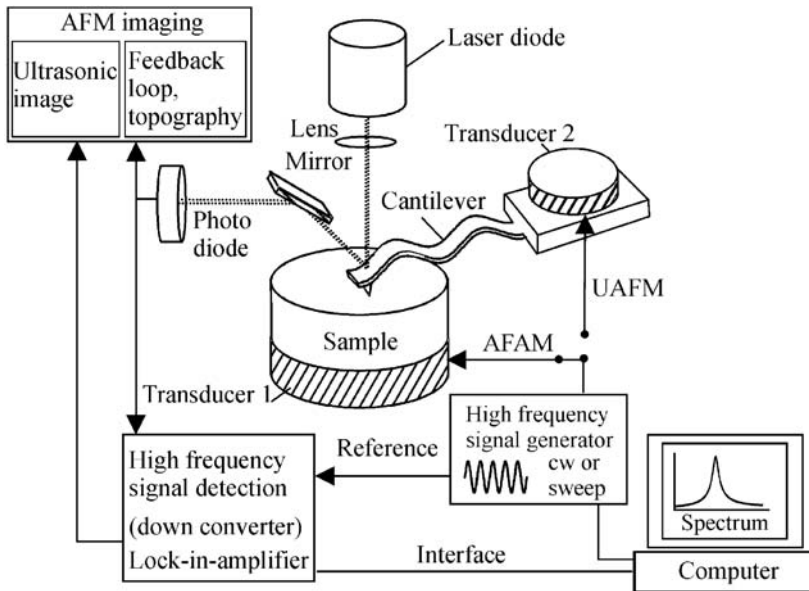


Fig. 2.1. In the AFAM-mode the flexural vibrations of the cantilever are excited by a transducer below the sample (*transducer 1*). The vibrations can also be excited by a transducer which excites the fixed end of the cantilever (*transducer 2*, UAFM-mode). The low frequency components of the beam deflection signal are used to control the static deflection of the cantilever. The high frequency components of the signal are evaluated for example by a lock-in-amplifier for ultrasonic spectroscopy or imaging

published by Yamanaka and Nakano and continuously developed afterwards [13, 54–56]. Alternatively, a ZnO transducer can be fabricated directly on the sensor beam to excite the vibrations in the UAFM-mode [57–59]. Dupas et al. fixed one end of the cantilever to a piezoelectric bimorph [60]. For simplicity the technique is designated here by AFAM or UAFM, when the vibrations are excited by the sample surface or by the fixed end of the beam, respectively. Excitation by a concentrated harmonic force acting directly on the cantilever [25] or spectral analysis of thermomechanical noise of the sensor [52, 53] is also reported for contact-resonance spectroscopy.

In the first AFAM experiments the ultrasonic transducer below the sample was excited with electrical spikes [61]. The resulting out-of-plane deflection of the investigated surface is a short pulse with a spectrum depending on the resonant frequency of the transducer and the transmission of the sample. The pulse at the surface excites a vibration in the cantilever which decays according to the time constants of contact damping and air damping. Fourier transformation of the cantilever vibrations showed that the spectrum contained contact resonances. However, with the pulse excitation the sensor tip loses contact with the sample surface very easily and the signals are strongly influenced by adhesion. The current state of the art in AFAM and UAFM is to excite the vibration with sinusoidal signals and to sweep the frequency to measure spectra. Frequency sweeps are also common in other dynamic AFM operation modes, but in the techniques discussed here the sensor tip is in contact with the

sample surface while the spectra are measured. This means that the static deflection of the cantilever must be controlled or monitored during the sweep. Furthermore, the techniques discussed here do not only use the fundamental resonant frequency of the cantilever but consider the higher modes, too.

The necessary bandwidth of excitation and detection depends on the type of sensor beam which is used. Softer samples like polymers can be examined with sensors having a spring constant of only a few N/m or less, while stiffer samples require stiffer beams with several 10 N/m spring constant. As will be shown in the following, for example the first contact-resonance frequency of the types of beams listed in Table 2.2 is always lower than 1 MHz. This means that ultrasonic imaging is possible with a bandwidth of 1 MHz. For quantitative evaluation, the bandwidth should be large enough to cover two contact resonances at a minimum.

The continuous wave signals are excited by a function generator. A fast lock-in amplifier can be used to determine amplitude and phase of the vibration of the cantilever. Alternatively, the ultrasonic signal and reference can be down converted to a lower frequency and reference (20 kHz) and subsequently fed to a lock-in-amplifier [62]. In this case the lock-in-amplifier works at a fixed lower frequency and needs not to follow the swept frequency. A network analyzer can also be used to excite and to detect the signals in spectral measurements [57]. Dupas et al. used a stroboscopic technique and increased the bandwidth of detection to 4 MHz by modulating the light intensity of the laser diode of the beam-deflection detector [60]. There are different possibilities of acoustical imaging using contact resonances which are discussed in Chap. 6.

2.2.1

Flexural Vibrations of Clamped-free Beams

The most widespread commercial cantilevers are either of triangular or of approximately rectangular shape. The vibrational modes for example of V-shaped beams or dagger-shaped beams can be calculated numerically [63, 64] or using analytical approximations [65]. However, analytical formulas can be evaluated extremely fast and they may provide a deeper understanding of how the different parameters influence the vibration. This analysis will therefore be restricted to cantilevers with approximately rectangular shape because they can be described with satisfactory precision by analytical models. Under the precondition that its length is much larger than its width and thickness, the micro fabricated sensor beam can be regarded as an elastic beam. If x is the coordinate in length direction of the beam and y the coordinate in thickness direction, the equation of motion for damped flexural vibrations becomes [66]:

$$EI \frac{\partial^4 y}{\partial x^4} + \eta_{\text{Air}} \rho A \frac{\partial y}{\partial t} + \rho A \frac{\partial^2 y}{\partial t^2} = 0 \quad (2.1)$$

where E is the Young's modulus of the cantilever, ρ is its mass density, A is the area of its cross section, I is the area moment of inertia and η_{Air} is a damping constant expressing the dissipation caused by the air. $y(x)$ is the deflection at position x , $\partial y / \partial x$ is the slope of the beam at position x , $E I \partial^2 y / \partial x^2$ is the torsional moment, and

$EI\partial^3 y/\partial x^3$ is the shear force. One seeks a harmonic solution in time with angular frequency $\omega = 2\pi f$. The solution of the differential equation of motion may be written:

$$y(x, t) = y(x) \cdot y(t) = (a_1 e^{\alpha x} + a_2 e^{-\alpha x} + a_3 e^{i\alpha x} + a_4 e^{-i\alpha x}) e^{i\omega t}. \quad (2.2)$$

The mode shape $y(x)$ can also be expressed as:

$$y(x) = A_1(\cos \alpha x + \cosh \alpha x) + A_2(\cos \alpha x - \cosh \alpha x) \\ + A_3(\sin \alpha x + \sinh \alpha x) + A_4(\sin \alpha x - \sinh \alpha x), \quad (2.3)$$

where a_1, a_2, a_3, a_4 and A_1, A_2, A_3, A_4 are constants. By substituting the solution (2.2) in the equation of motion (2.1) one obtains the dispersion relation for a flexural wave with complex wave number α :

$$EI\alpha^4 + i\rho A\eta_{\text{Air}}\omega - \rho A\omega^2 = 0 \quad (2.4)$$

$$\alpha_{\pm} = \pm \sqrt[4]{\frac{\rho A}{EI}(\omega^2 \mp i\eta_{\text{Air}}\omega)}. \quad (2.5)$$

In absence of damping the dispersion equation simplifies to:

$$f = \frac{(\alpha L)^2}{2\pi} \frac{1}{L^2} \sqrt{\frac{EI}{\rho A}}. \quad (2.6)$$

Boundary conditions must be fulfilled if the beam is of finite length L . By substituting the boundary conditions in the general solution one obtains a characteristic equation. For a beam with one clamped end and one free end one finds in textbooks [66,67]:

$$\cos \alpha L \cosh \alpha L + 1 = 0 \quad (2.7)$$

The roots $\alpha_n L$ of this equation can be calculated numerically, where $n = \{1, 2, 3, \dots\}$ is the mode number. Examples are listed in Table 2.1. Using the dispersion relation one obtains the resonant frequencies of the beam. The quality factor Q of the resonances is given by:

$$Q = \frac{\omega_n}{\Delta\omega} = \frac{\omega_n}{\eta_{\text{Air}}} \quad (2.8)$$

According to (2.8), the quality factor Q increases with the mode number. Experimentally one often observes an increase in Q for the first modes up to 1 MHz followed by a decrease at still higher frequencies [44]. This means that the damping η_{Air} is in fact a function of the frequency. Quality factors of the first flexural resonances of commercial sensors in air are typically between $Q = 200$ and $Q = 900$ for sensors made of single crystal silicon.

With most commercial atomic force microscopes the cantilever can be excited to forced vibration when its one end is free. The fundamental mode of the clamped-free beam and the quality factor of the resonance can be measured in this way. On the

Table 2.1. Dimensionless wave number $\alpha_n L$ and frequency ratio $f_n/f_{1,\text{free}}$ for different boundary conditions of the beam: clamped-free ($f_{n,\text{free}}$), clamped-pinned ($f_{n,\text{pin}}$), and clamped-clamped ($f_{n,\text{clamp}}$)

n	$(\alpha_n L)_{\text{free}}$	$f_{n,\text{free}}/f_{1,\text{free}}$	$(\alpha_n L)_{\text{pin}}$	$f_{n,\text{pin}}/f_{1,\text{free}}$	$(\alpha_n L)_{\text{clamp}}$	$f_{n,\text{clamp}}/f_{1,\text{free}}$
1	1.87510	1.00	3.92660	4.39	4.73004	6.36
2	4.69409	6.27	7.06858	14.21	7.85320	17.54
3	7.85476	17.55	10.21018	29.65	10.99561	34.39
4	10.99554	34.39	13.35177	50.70	14.13717	56.84
5	14.13717	56.84	16.49336	77.37	17.27876	84.91
6	17.27876	84.91	19.63495	109.65	20.42035	118.60
7	20.42035	118.60	22.77655	147.55	23.56194	157.90
	$\approx \frac{2n-1}{2}\pi$		$\approx \frac{4n+1}{4}\pi$		$\approx \frac{2n+1}{2}\pi$	

other hand, the constants ρ , A , E , I , and η_{Air} are often unknown. It is therefore better to rewrite the dispersion relations (2.5) and (2.6) in terms of measurable quantities:

$$\begin{aligned} \alpha_{\pm} L &= \pm \alpha_{1,\text{free}} L \cdot \sqrt[4]{\frac{\omega^2}{\omega_{1,\text{free}}^2} \mp i \frac{\eta_{\text{Air}} \omega}{\omega_{1,\text{free}}^2}} \\ &\approx \pm 1.8751 \cdot \sqrt[4]{\left(\frac{f}{f_{1,\text{free}}}\right)^2 \mp i \frac{1}{Q_{1,\text{free}}} \frac{f}{f_{1,\text{free}}}} \end{aligned} \quad (2.9)$$

$$\frac{f}{f_{1,\text{free}}} = \frac{(\alpha L)^2}{(\alpha_{1,\text{free}} L)^2}. \quad (2.10)$$

Due to the high quality factors Q of the flexural modes in air the shift of the resonant frequencies caused by air damping is negligible. Here the resonant frequencies of the clamped-free beam are sometimes called “free” resonances. In this case “free vibration” is not meant as the opposite of “forced vibration” but relates to the end condition of the beam. The theory predicts a certain ratio of the free flexural resonant frequencies regardless of the cross section and the length of the beam, for example:

$$\frac{f_{2,\text{free}}}{f_{1,\text{free}}} = \frac{(4.6941)^2}{(1.8751)^2} = 6.27. \quad (2.11)$$

The first ten solutions $\alpha_n L$ for the clamped-free beam without damping ($\eta_{\text{Air}} = 0$) are listed in Table 2.1. Note that the bending modes are not equidistant in frequency. According to the dispersion equation, the frequency ω is not proportional to the wave number α , but $\omega \sim \alpha^2$. For the higher modes the frequency interval to the next higher mode increases with the square of the frequency. The higher bending modes are no harmonics of the fundamental frequency.

2.2.2

The Point-mass Model

It is very common in atomic force microscopy to approximate the fundamental flexural mode of the clamped-free beam by a harmonic oscillator (Fig. 2.2). The constants of a point-mass model are chosen such that the resonant frequency of the harmonic oscillator ω_0 equals the first resonant frequency of the beam $\omega_{1,\text{free}}$:

$$\omega_{1,\text{free}} = \sqrt{\frac{k_C}{m^*}} \equiv \omega_0 \quad (2.12)$$

The static spring constant k_C of the cantilever for forces acting at $x = L$ is:

$$k_C = \frac{3EI}{L^3} = \frac{Eb^3w}{4L^3} \quad (2.13)$$

The second expression holds for rectangular beams, where w and b are the width and thickness, respectively. The effective mass m^* is now calculated according to

$$m^* = \frac{k_C}{\omega_{1,\text{free}}^2} = \frac{3\rho Lwb}{(\alpha_{1,\text{free}}L)^4} \approx \frac{1}{4}m \quad (2.14)$$

Here m is the real mass of the cantilever. The motion of the beam at the free end ($x = L$) can now be described by the equation of motion of a point-mass m^* :

$$m^* \ddot{y}(L, t) + m^* \eta_{\text{Air}} \dot{y}(L, t) + k_C y(L, t) = 0 \quad (2.15)$$

Interaction between the sensor tip located at $x = L$ and a sample surface gives rise to forces, which can be represented by a second spring with the stiffness k^* . The second spring leads to a change of the resonant frequency of the system according to [44, 68, 69]:

$$\omega = \sqrt{\frac{k^* + k_C}{m^*}} = \omega_0 \sqrt{1 + \frac{k^*}{k_C}} \quad (2.16)$$

It has been shown that the point-mass model fails to predict quantitatively correct amplitudes and resonant frequencies when the contact stiffness k^* is of the same order of magnitude or larger than the static spring constant k_C of the sensor [70]. Nevertheless, the fundamental frequency of the clamped-free beam ω_0 or $f_0 = \omega_0/2\pi$, the static spring constant k_C , and the effective mass m^* are very useful to characterize a sensor.

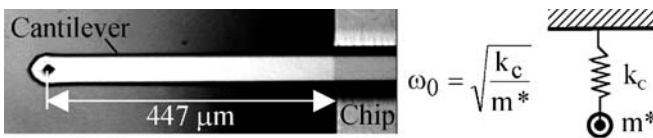


Fig. 2.2. Optical micrograph of an AFM cantilever and point-mass model

2.2.3

Experiments with Clamped-free Beams

With respect to application it is important to examine how well real sensors correspond to the flexural beam model. It is helpful to use a calibrated optical interferometer with a bandwidth of several MHz to examine as many of the higher modes of the cantilever as possible [44, 71]. For example, Hoummady et al. examined higher flexural modes of AFM cantilevers interferometrically in order to use them for imaging [72] and Cretin and Vairac used an optical interferometer to measure the vibration of the sensor in SMM [36].

Figure 2.3 shows a set-up with a Michelson-heterodyne interferometer [73]. The chip at which the cantilever is fixed is glued to an ultrasonic transducer (shear wave transducer V155, 5 MHz center frequency, Panametrics-NDT, Waltham, MA, USA). The transducer is excited with a function generator (model 33120A, Agilent Technologies). Due to the high quality factors Q of its modes, peak-to-peak voltages of several volts are sufficient to excite vibration amplitudes of the beam of several nm or even several 10 nm. Though a longitudinal wave transducer excites flexural waves more effectively, the shear wave transducer was chosen because it excites as many types of modes as possible. Torsional resonances and lateral modes could be examined in this way, too. Depending on the dimensions and material constants of the beam, it can happen that for example a torsional mode and a flexural mode have almost the same frequency. Such a situation leads to mode coupling [71, 74] and consequently to difficulties in quantitative evaluation. The He – Ne Laser beam of the interferometer is focused onto the cantilever with a microscope objective. The resulting spot diameter is only a few μm . The cantilevers are mounted on a motor-driven x - y table to scan their surface with the help of two stepper motors.

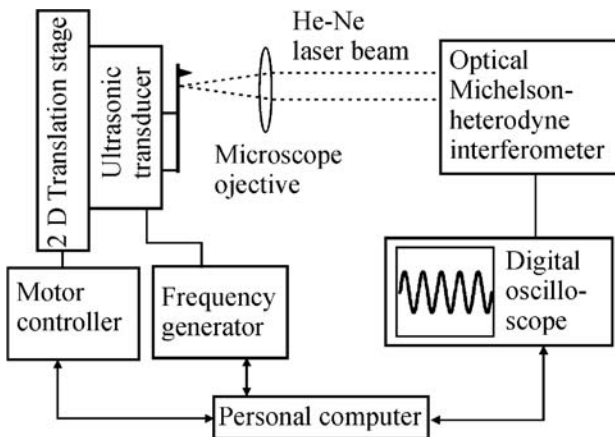


Fig. 2.3. Set-up of the optical interferometer to measure the amplitudes of the clamped-free cantilever vibration modes. The chip of the cantilever is glued to an ultrasonic transducer which provides an excitation of vibration up to a few MHz. The laser beam of the interferometer is focused onto the cantilever to a spot size of a few μm . Step motors controlled by a computer scan the surface of the cantilever

Knowledge of the two-dimensional mode shape helps to identify modes which appear as unknown peaks in the resonance spectrum. The interferometer signal is read with a digital oscilloscope, amplitude and phase of the vibration are obtained by fast Fourier transformation. A three dimensional visualization of such a measurement is shown in Fig. 2.4.

A spectral analysis showed that the beams made of silicon single crystal behaved linearly at vibration amplitudes of a few ten nm, i.e. they vibrated only at the frequency of excitation. After measurement of the fundamental mode the higher resonant frequencies of the clamped-free beam can be predicted with the frequency ratios in Table 2.1. Usually the values calculated in this way are close enough to the experimental frequencies to detect the higher modes easily. In detail, however, there are systematic deviations from the theory which depend on the type of beam. The deviations from theory can be visualized by dividing the frequencies of the higher modes by the theoretical ratio $f_{n,\text{free}}/f_{1,\text{free}}$ and plotting them as a function of mode number. In case of perfect correspondence of the sensor with the model such a plot would provide a horizontal line.

Figures 2.5a and b show the resonant frequencies of a number of silicon beams. Typical dimensions of the beams examined here are listed in Table 2.2 The absolute resonant frequencies of the beams vary because of thickness variations of the

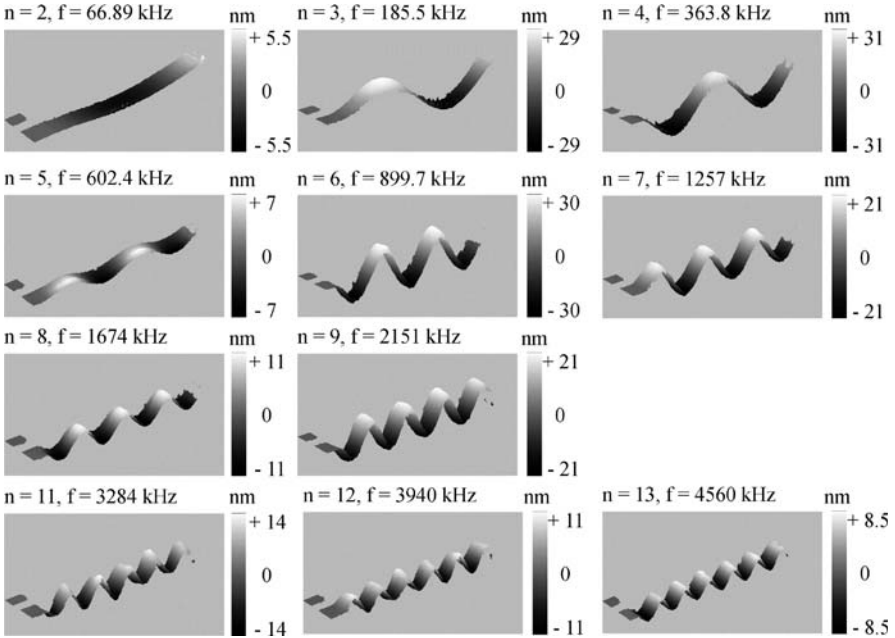


Fig. 2.4. Bending modes of a cantilever made of single crystal silicon measured with an optical interferometer in air. The frequency of the first mode was below detection limits of the interferometer. Mode $n = 10$ was not detected for unknown reasons. The dimensions of the beam were $1.61 \times 45 \times 440 \mu\text{m}^3$ (thickness \times width \times length) and the static spring constant was $k_C = 0.094 \text{ N/m}$ according to the manufacturer

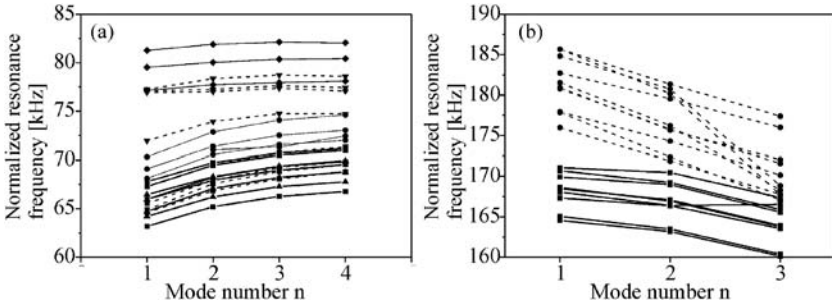


Fig. 2.5. (a) Resonant frequencies of the first four flexural modes of 23 cantilevers from 6 different wafers (type FM, Nanosensors). (b) Resonant frequencies of the first three flexural modes of 19 cantilevers from two different wafers (type NCL, Nanosensors). The frequencies of the higher modes were divided by the theoretical frequency ratio f_n/f_0 . Modes of each individual beam are connected by a *line*. The same symbol and line type was used for beams from the same wafer. In case of perfect correspondence to the flexural beam model, the frequencies would be connected by *horizontal lines*. The strong deviations in (b) were caused by *multiple peaks*

Table 2.2. Typical data of single crystal silicon cantilevers used here as provided by the manufacturer (Nanosensors, NanoWorld AG, Neuchatel, Switzerland). The cantilevers are of approximately rectangular shape. The cross-section of the beams is trapezoidal

Type of beam	Length L [μm]	Width w [μm]	Thickness b [μm]	Spring constant k_C [N/m]	Resonant frequency [kHz]
NCL	215–235	20–45	6–8	21–98	146–236
FM	215–235	20–35	2–4	0.5–9.5	45–115
CONT	440–460	42.5–57.5	1–3	0.02–0.77	6–21

silicon wafers used for manufacturing. Furthermore, for one type of beam (FM) the frequencies increase more strongly, while for another type (NCL) they increase less with the mode number than predicted by the model. These systematic deviations are caused by details which are not considered in the simple analytical model. For example the beams are made of mechanically anisotropic material, the clamping of the fixed end is not infinitely stiff and symmetric, and the cross-section of the beams is not constant. The influence of these details on the resonant frequencies can be examined theoretically by finite-element calculations [75]. For example Hurley et al. examined the deviations caused by a triangular end of the beam (dagger shape) [64].

Another practical problem which often occurs when resonant frequencies are measured in an AFM is double peaks or even multiple peaks. Mode coupling can only happen if two modes have frequencies close to each other. Therefore it is likely that most of the unwanted maxima in the spectrum are caused by maxima which are already present in the spectrum of the vibration which excites the beam. The spectrum of the forced linear vibration is a product of the vibration spectrum of the chip and the spectrum of the cantilever. The chip of the cantilever has typical dimensions of $4 \times 2 \times 0.5 \text{ mm}^3$ (length \times width \times thickness) and is therefore a mechanical structure with numerous resonant frequencies. The exact spectrum depends on how

the chip is clamped [75]. In the AFAM-mode ultrasonic waves transmitted through a sample generate the surface vibration, which means that in this case the spectrum of the exciting signal depends on the material, the dimensions, and the clamping of the sample.

2.3

Contact Forces as Linear Springs and Dashpots

When the sensor tip is in contact with a sample surface, the tip-sample forces change the end conditions of the beam. Figure 2.6 shows the situation schematically. The tip-sample forces are a nonlinear function of the tip-sample separation and they can also be hysteretic. Here it is assumed that the vibration amplitudes are so small that the forces can be represented by a system of linear springs and dashpots. In case of bending modes one can treat the problem in only two dimensions. There are forces normal to the surface represented by the normal contact stiffness k^* and the contact damping γ and forces lateral to the surface represented by the lateral contact stiffness k_{Lat}^* and a lateral contact damping γ_{Lat} . For technical reasons the cantilever is tilted with respect to the surface by an angle φ (11° to 15°), i.e. the coordinate system of the surface is rotated by φ with respect to the coordinate system of the cantilever.

The normal and lateral contact stiffness can be calculated from contact mechanics models [74,76,77]. Depending on the material of which tip and surface are made, all sorts of physical forces, including magnetic and electrostatic forces, can contribute to the contact stiffness. The different force models will not be discussed in detail here, but it will be assumed that the surface preparation was such that elastic forces prevail. Though in principle all types of forces can be measured by AFAM, predominance of elasticity can be ensured by choosing high enough static loads applied by the cantilever (several 100 nN).

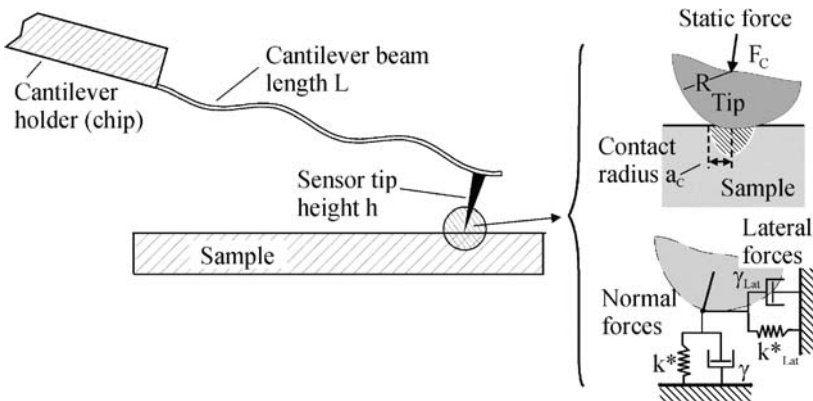


Fig. 2.6. The sensor tip is in contact with the sample surface. A contact area of radius a_c forms between the tip and the surface and the tip senses forces lateral and normal to the sample surface which are modeled by *linear springs* and *dashpots*

The Hertzian model describes the contact between two nonconforming elastic bodies of general anisotropy [78]. In the simplest case the bodies are mechanically isotropic, the sample is considered as flat and the sensor tip is represented by a sphere with a radius R . If a normal force F_n acts onto the sphere, a contact radius a_C forms:

$$a_C = \sqrt[3]{3F_n R / 4E^*} . \quad (2.17)$$

If the adhesion forces are so small that they can be neglected, the normal force F_n is given by the static deflection of the cantilever multiplied with the spring constant of the cantilever. The sum of the indentation in the contacting bodies, δ_n , i.e. the amount the two bodies approach is given by:

$$\delta_n = \sqrt[3]{\frac{9F_n^2}{16RE^{*2}}} , \quad (2.18)$$

The normal contact stiffness k^* is:

$$k^* = 2a_C E^* = \sqrt[3]{6E^{*2} R F_n} . \quad (2.19)$$

Here, E^* is the reduced Young's modulus of the contact which is given by

$$\frac{1}{E^*} = \frac{(1 - \nu_S^2)}{E_S} + \frac{(1 - \nu_T^2)}{E_T} , \quad (2.20)$$

where E_S , E_T , ν_S , ν_T , are Young's modulus and Poisson's ratio of the surface and the tip, respectively. After AFAM experiments, the tip shape often deviates from that of a sphere [79]. In this case the shape of the tip can be described more generally by a body of revolution. It has been shown that for axisymmetric indenters on elastically isotropic half spaces the contact stiffness k^* , i.e. the derivative of the applied load F_n with respect to the indentation depth, δ_n , generally obeys the equation [80]:

$$k^* = \frac{dF_n}{d\delta_n} = \frac{2}{\sqrt{\pi}} \sqrt{S E^*} \quad (2.21)$$

Here $S = \pi \times a_C^2$ is the contact area. Therefore the relation

$$E^* = k^* / (2a_C) , \quad (2.22)$$

which can be derived from the Hertzian model, still holds in this more general case. These formulas are derived on the assumptions of a frictionless contact. The Hertzian model is only valid if the contact area is small compared with the dimensions of the contacting bodies and their radii of curvature [78], which means that the contact radius must be smaller than the tip radius $a_C \ll R$. Linear elastic theory is only valid if the mechanical stresses remain small enough. In AFM these two conditions are easily violated when a sensor tip with a radius of a few nm contacts a metallic or ceramic sample surface.

The contact radius defines the lateral resolution in contact-resonance spectroscopy. A typical contact radius in AFM ranges from several nm up to several tens of nanometers, depending on the tip radius and the elasticity of the tip and the sample. Many polycrystalline materials like metals and ceramics, which appear mechanically homogeneous on a macroscopic scale, show a local variation in elastic constants for a scanning probe microscope because the tip senses the individual grains within the polycrystalline aggregate. Each grain represents a small single crystal. This means that imaging by AFM can only be explained when the sample surface is no longer treated as an isotropic material. Furthermore AFM sensor tips made of single crystalline silicon are not elastically isotropic, and this holds for other tip materials as well. Mechanically anisotropic materials are described by more than two elastic constants. In the most general case of two non-conforming bodies of general shape and anisotropy, the contact area is elliptical [78]. The reduced Young's modulus of the contact is a function of the indentation δ_n , contains combinations of the elastic constants of tip and sample and cannot be separated into a sum of a contribution from tip and surface like in (2.20). Vlassak and Nix examined the indentation of a rigid parabolic punch in an anisotropic surface [81]. They showed that the contact area remains spherical if a three- or fourfold rotational symmetry axis perpendicular to the boundary exists. In this case (2.19) and (2.21) remain valid if the isotropic reduced elastic modulus $E/(1 - \nu^2)$ is replaced by an indentation modulus that is calculated numerically from single crystal elastic constants [82]. Equation (2.20) is replaced by:

$$\frac{1}{E^*} = \frac{1}{M_S} + \frac{1}{M_T} \quad (2.23)$$

where M_S and M_T are the indentation modulus of the sample and the tip, respectively. The required symmetry holds for silicon sensor tips which are oriented in (001) crystallographic direction. Because of its fourfold symmetry the tip does not alter the rotational symmetry if it is in vertical contact with an isotropic body or with a sample which also has a fourfold rotational symmetry axis along the tip and indentation axis. Even for bodies which do not have a three- or fourfold symmetry axis (2.23) can be used as a first approximation. The error made by application of this equation depends on the anisotropy and can be estimated [83].

The tilt angle φ of the cantilever causes tip-sample forces tangential to the surface when the surface is moved in its normal direction. Additionally, the flexural vibrations cause an angular deflection $\partial y/\partial x$ at the sensor-tip position and consequently a lateral deflection $h\partial y/\partial x$ of the sensor tip apex. Tangential forces were treated by Mindlin [78]. The lateral contact stiffness depends on the effective shear stiffness G^* of the contact:

$$k_{\text{Lat}}^* = \frac{dF_L}{d\delta_L} = 8a_C G^* \quad (2.24)$$

$$\frac{1}{G^*} = \frac{2 - \nu_S}{G_S} + \frac{2 - \nu_T}{G_T} \quad (2.25)$$

where δ_L is the lateral contact deflection, and G_S and G_T are the shear modulus of the sample and the tip, respectively. For isotropic bodies the ratio between the normal contact stiffness k^* and the lateral contact stiffness k_{Lat}^* is independent of the

normal force F_n :

$$\frac{k_{\text{Lat}}^*}{k^*} = \frac{8a_C G^*}{2a_C E^*} = \frac{4G^*}{E^*}. \quad (2.26)$$

As Mazeran and Loubet pointed out [25], for $E_T \gg E_S$

$$\frac{k_{\text{Lat}}^*}{k^*} \approx \frac{2(1 - \nu_S)}{2 - \nu_S}. \quad (2.27)$$

Taking a range of Poisson's ratio from 0.1 for diamond to 0.5 for rubber, the ratio of lateral and normal contact stiffness k_{Lat}^*/k^* varies from 2/3 to 18/19 with an average value of 0.85 [25]. Like in the case of the normal contact stiffness, it will be necessary in future to calculate shear stiffness, taking into account the mechanical anisotropy of the contacting bodies.

An important question for nondestructive testing is whether techniques like AFAM or UAFM are able to detect sub-surface features. The typical frequency f of ultrasonic excitation is 100 kHz to 10 MHz. The velocity of longitudinal acoustic waves in the solids under examination ranges typically from $v = 1 \text{ mm}/\mu\text{s}$ (polymers) to $v = 10 \text{ mm}/\mu\text{s}$ (ceramics). In this case the acoustic wavelength $\lambda = v/f$ ranges from $100 \mu\text{m}$ to 10 cm . Consequently the acoustic wavelength is larger than the scan width of the AFM and orders of magnitude larger than the contact radius. This confirms that the vibrating tip can be seen like a dynamic indenter and the penetration depth of the ultrasonic techniques is given by the decay of the mechanical stress field in the sample.

According to the Hertzian contact model the decay length is several multiples of the contact radius (see Fig. 2.7). Therefore it is possible to measure the film thickness with AFAM or UAFM [57], provided the films are thin enough. Yaralioglu et al. calculated the contact stiffness of layered materials using the impedance of a mechanical radiator [58]. They examined thin films of photo resist, W, Al, and Cu on silicon single crystal. They were able to show that in the low frequency limit ($f \rightarrow 0$) the impedance method provides the same results for the contact stiffness k^* as the Hertzian contact model and that this method is well suited to

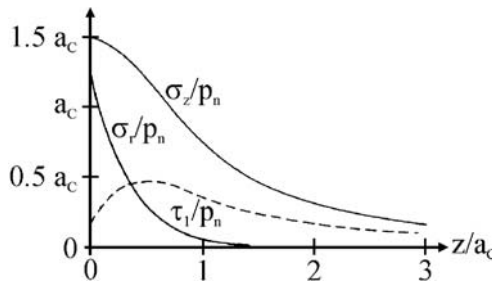


Fig. 2.7. Mechanical stress field in a Hertzian contact as a function of penetration depth z into the surface. The average normal pressure p_n in the contact area is given by $p_n = F_n/\pi a_C^2$, where F_n is the normal force and a_C is the contact radius. The compressional stresses σ_z and σ_r have their maximum at the surface and the principal shear stress τ_1 reaches its maximum in the sample [78]

calculate the influence of subsurface defects on the contact stiffness [84]. Tsuji et al. observed subsurface dislocation movement in graphite with UAFM. They calculated the influence of a subsurface layer with lower Young's modulus on the contact stiffness using finite elements [85–88]. The penetration depth of the mechanical stress field can be enhanced by increasing the contact radius, however, this causes a loss in lateral resolution. According to Fig. 2.7 the compressional stress has its maximum at the sample surface, while the shear stress reaches its maximum below the surface. Therefore techniques which exploit lateral vibrations like torsional contact-resonance spectroscopy should be very sensitive to subsurface defects.

2.4

Characteristic Equation of the Surface-coupled Beam

In the linear model shown in Fig. 2.8 the forces between the sensor tip and the surface are represented by a system of springs and dashpots. The length of the cantilever from the clamped end to the free end is L . The sensor tip is located at position L_1 and $L_2 = L - L_1$ is the distance between the tip position and the free end. Again, one seeks a harmonic solution in time. Two sections of the cantilever with individual solutions for the mode shapes, $y_1(x_1)$ and $y_2(x_2)$, respectively, are defined. The function $y_1(x_1)$ describes the amplitude of the section which begins at the clamped end at $x = 0$ and ends at the tip position at $x = L_1$. For simplicity one can use $y(x)$ instead of $y_1(x_1)$, because the two functions are identical on the first section of the beam. The function $y_2(x_2)$ begins at the free end of the beam and ends at the tip position at $x_2 = L_2$. At the clamped end of the beam the deflection and the slope of

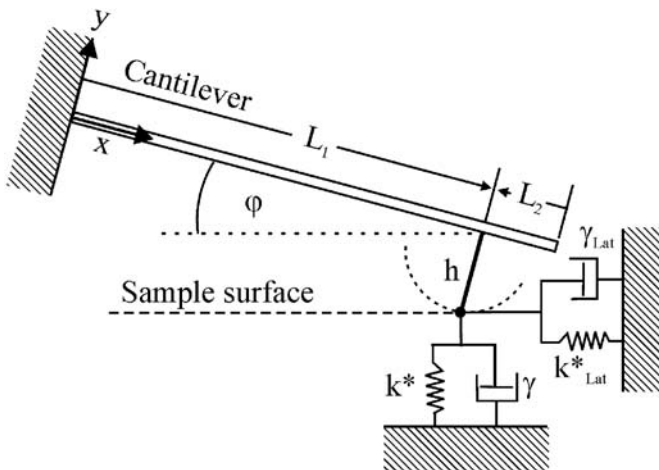


Fig. 2.8. Linear model of the cantilever when the sensor tip is in contact with a sample surface. The tip-sample interaction forces are represented by *springs* and *dashpots*. The cantilever is tilted by an angle φ with respect to the surface. The sensor tip of height h is located at a position L_1 on the length axis of the cantilever. The distance of the tip to the free end of the cantilever is L_2

the beam must be zero, while at the free end of the beam the forces and moments have to be zero. The end conditions for $y(x)$ and $y_2(x_2)$ are therefore:

$$x = 0 : \begin{cases} y(x) = 0 \\ \frac{\partial y(x)}{\partial x} = 0 \end{cases} \quad y = L : \begin{cases} \frac{\partial^2 y}{\partial x^2} = 0 \\ \frac{\partial^3 y}{\partial x^3} = 0 \end{cases} . \quad (2.28)$$

The solution (2.3) and its derivatives together with the foregoing end conditions yield $A_1 = A_3 = 0$ for $y(x)$ and $A_2 = A_4 = 0$ for $y_2(x_2)$. The shape functions therefore have the form:

$$\begin{aligned} y(x) &= A_2(\cos \alpha x - \cosh \alpha x) + A_4(\sin \alpha x - \sinh \alpha x) \\ y_2(x_2) &= A_1(\cos \alpha x_2 + \cosh \alpha x_2) + A_3(\sin \alpha x_2 + \sinh \alpha x_2) . \end{aligned} \quad (2.29)$$

The partial solutions $y(x)$ and $y_2(x_2)$ must be coupled continuously at the tip position at $x = L_1$ i.e. at $x_2 = L_2$.

$$x = L_1 \quad \text{or} \quad x_2 = L_2 : \begin{cases} y(x) = y_2(x_2) \\ \frac{\partial y(x)}{\partial x} = -\frac{\partial y_2(x_2)}{\partial x_2} \end{cases} \quad (2.30)$$

The negative sign in the equation for the derivatives appears because the x_2 -axis is defined in the negative direction of the x -axis. This direction was only chosen for convenience of calculation. Note that the x -axis (and the x_2 -axis) of the cantilever is not parallel to the surface when the cantilever is tilted by an angle φ as shown in Fig. 2.8. In this text the terms “ y -axis” and “ x -axis” always correspond to the coordinate system of the cantilever. The moments and the forces on the sensor tip lead to further boundary conditions at the coupling position. One can first consider a simplified case where the x -axis of the cantilever is parallel to the sample surface and only forces normal to the surface are acting ($\varphi = 0$, $k_{\text{Lat}}^* = 0$, and $\gamma = 0$). The boundary condition for the shear forces at $x = L_1$ is in this case:

$$EI \frac{\partial^3 y}{\partial x^3} + EI \frac{\partial^3 y_2}{\partial x_2^3} = k^* y(L_1, t) + \gamma \frac{\partial y(L_1, t)}{\partial t} . \quad (2.31)$$

The solution looked for is a harmonic wave of the form $y(x, t) = y(x) \exp(i\omega t)$. The time derivatives can therefore be calculated and reformulated using the dispersion relation (2.6) neglecting the air damping. This leads to the boundary condition

$$\begin{aligned} \frac{\partial^3 y}{\partial x^3} + \frac{\partial^3 y_2}{\partial x_2^3} &= \frac{1}{EI} \cdot (k^* y(L_1, t) + \gamma i \omega y(L_1, t)) \\ &= y(L_1, t) \left(\frac{k^*}{EI} + \gamma i \alpha^2 \sqrt{\frac{1}{EI \rho A}} \right) . \end{aligned} \quad (2.32)$$

A contact function $\phi(\alpha)$ is defined, which contains contact stiffness and contact damping:

$$\phi(\alpha) = 3 \frac{k^*}{k_C} + i(\alpha L_1)^2 p. \quad (2.33)$$

The spring constant k_C of the cantilever (2.13) was used. The dimensionless damping constant p is defined as [70]:

$$p = \frac{L_1 \gamma}{\sqrt{EI\rho A}} = \frac{L_1}{L} \frac{3\gamma}{(1.875)^2 m^* \omega_0} = \frac{L_1}{L} \frac{(1.875)^2 \gamma}{m \omega_0}. \quad (2.34)$$

Substituting the contact function $\phi(\alpha)$ in (2.31), the boundary condition now becomes

$$\frac{\partial^3 y}{\partial x^3} + \frac{\partial^3 y_2}{\partial x_2^3} = \frac{\phi(\alpha)}{L_1^3} y(L_1). \quad (2.35)$$

In the same way a lateral contact function $\phi(\alpha)_{\text{Lat}}$ is defined:

$$\phi_{\text{Lat}}(\alpha) = 3 \frac{k_{\text{Lat}}^*}{k_c} + i(\alpha L_1)^2 p_{\text{Lat}} \quad p_{\text{Lat}} = \frac{L_1 \gamma_{\text{Lat}}}{\sqrt{EI\rho A}}. \quad (2.36)$$

The angle φ of the cantilever with relation to the surface causes cross-coupling between lateral and normal signals. Forces F_x in length-direction of the beam acting on the sensor tip give rise to a moment $M = hF_x$ at the end of the beam. The angular deflection $\partial y/\partial x$ of the beam at the tip position causes a deflection in x -direction $h\partial y/\partial x$ of the tip apex. In summary, this leads to the following boundary conditions for the forces and the moments at the tip position:

$$x = L_1 \quad \text{or} \quad x_2 = L_2: \quad \begin{cases} \frac{\partial^2 y(x)}{\partial x^2} - \frac{\partial^2 y_2(x_2)}{\partial x_2^2} = -T(\alpha) \frac{\partial y(x)}{\partial x} - X(\alpha) y(x) \\ \frac{\partial^3 y(x)}{\partial x^3} + \frac{\partial^3 y_2(x_2)}{\partial x_2^3} = U(\alpha) \cdot y(x) + X(\alpha) \frac{\partial y(x)}{\partial x} \end{cases}. \quad (2.37)$$

The auxiliary functions T , X and U are defined as follows:

$$\begin{aligned} T(\alpha) &= \frac{h^2}{L_1^3} \phi(\alpha) \sin^2 \varphi + \frac{h^2}{L_1^3} \phi_{\text{Lat}}(\alpha) \cos^2 \varphi \\ X(\alpha) &= \frac{h}{L_1^3} \sin \varphi \cdot \cos \varphi [\phi_{\text{Lat}}(\alpha) - \phi(\alpha)] \\ U(\alpha) &= \frac{1}{L_1^3} \phi(\alpha) \cos^2 \varphi + \frac{1}{L_1^3} \phi_{\text{Lat}}(\alpha) \sin^2 \varphi. \end{aligned} \quad (2.38)$$

The four boundary conditions at the coupling position are used to determine the four unknown constants in the shape functions $y(x)$ and $y_2(x_2)$. The solutions of this eigenvalue problem define an infinite set of discrete wave numbers α_n . After some

pages of calculation one obtains the following characteristic equation:

$$\Omega(\alpha) \equiv S_4 + S_3 T(\alpha) + S_2 X(\alpha) + S_1 U(\alpha) + S_0 [T(\alpha)U(\alpha) - X^2(\alpha)] = 0 \quad (2.39)$$

where S_0 , S_1 , S_2 , S_3 , and S_4 stand for the following terms:

$$S_0 = (1 - \cos \alpha L_1 \cosh \alpha L_1)(1 + \cos \alpha L_2 \cosh \alpha L_2)$$

$$S_1 = \alpha [-(1 - \cos \alpha L_1 \cosh \alpha L_1)(\sin \alpha L_2 \cosh \alpha L_2 - \sinh \alpha L_2 \cos \alpha L_2) \\ + (1 + \cos \alpha L_2 \cosh \alpha L_2)(\sin \alpha L_1 \cosh \alpha L_1 - \sinh \alpha L_1 \cos \alpha L_1)]$$

$$S_2 = 2\alpha^2 [\sin \alpha L_1 \sinh \alpha L_1 (1 + \cos \alpha L_2 \cosh \alpha L_2) \\ + \sin \alpha L_2 \sinh \alpha L_2 (1 - \cos \alpha L_1 \cosh \alpha L_1)]$$

$$S_3 = \alpha^3 [(\sin \alpha L_1 \cosh \alpha L_1 + \sinh \alpha L_1 \cos \alpha L_1)(1 + \cos \alpha L_2 \cosh \alpha L_2) \\ - (\sin \alpha L_2 \cosh \alpha L_2 + \sinh \alpha L_2 \cos \alpha L_2)(1 - \cos \alpha L_1 \cosh \alpha L_1)]$$

$$S_4 = 2\alpha^4 (1 + \cos \alpha L \cosh \alpha L) \quad (2.40)$$

The last term in the characteristic equation (2.39) can be further simplified by substituting the definitions of the auxiliary functions:

$$T(\alpha)U(\alpha) - X^2(\alpha) = \frac{h^2}{L_1^6} \phi(\alpha) \phi_{\text{Lat}}(\alpha) \quad (2.41)$$

2.4.1

Discussion of the Characteristic Equation

In order to understand the characteristic equation of the surface-coupled beam, it is helpful to consider simple cases. If for example all the spring constants and the dashpot constants are set to zero, the auxiliary functions $T(\alpha)$, $X(\alpha)$, and $U(\alpha)$ become zero too. This means that all terms except S_4 vanish in $\Omega(\alpha)$ and the characteristic equation reduces to (2.7) which is the equation of the clamped-free beam.

As a next step one can consider only a normal spring k^* , the lateral spring constant and the contact damping are still considered to be zero. This means that the contact function and the lateral contact function become $\phi(\alpha) = 3k^*/k_C$ and $\phi_{\text{Lat}}(\alpha) = 0$, respectively. If in addition the beam is not tilted ($\varphi = 0$), and if the tip is located at the end of the beam ($L_1 = L$ and $L_2 = 0$), the auxiliary functions $X(\alpha)$ and $T(\alpha)$ vanish and $U(\alpha)$ simplifies to $U(\alpha) = \phi(\alpha) = 3k^*/k_C$. The characteristic equation for a clamped-spring-coupled beam [13, 44] then follows:

$$(\alpha L)^3 (1 + \cos \alpha L \cosh \alpha L) + 3 \frac{k^*}{k_C} (\sin \alpha L \cosh \alpha L - \sinh \alpha L \cos \alpha L) = 0 \quad (2.42)$$

Two examples of the shape function $y(x)$ of this case are shown in Fig. 2.9. Note that (2.42) contains the characteristic equation of the clamped-free beam and the characteristic equation of the clamped-pinned beam, combined by the factor $(\alpha L)^3 k_C / 3k^*$. The clamped-pinned case is reached when the normal contact stiffness k^* goes to infinity.

Starting from the clamped-pinned case one can now add a lateral spring which causes feedback forces proportional to the angle of the end of the beam. A lateral spring fixed to the sensor tip is equivalent to a torsional spring which is fixed directly to the end of the beam [25]. The characteristic equation of this case can be obtained by dividing (2.39) by $U(\alpha)$ and subsequently considering the case $U(\alpha) \rightarrow \infty$. From the remaining terms $S_1 + S_0 T(\alpha) = 0$ one obtains the following characteristic equation:

$$3 \frac{h^2 k_{\text{Lat}}^*}{L^2 k_C} (1 - \cos \alpha L \cosh \alpha L) + \alpha L (\sin \alpha L \cosh \alpha L - \sinh \alpha L \cos \alpha L) = 0 \quad (2.43)$$

Finally, when the lateral spring constant too goes to infinity, one obtains a cantilever which is clamped at both ends. The simplified cases of the characteristic equation discussed above are shown in Fig. 2.9. Furthermore, the shapes of the first ($n = 1$) and the third ($n = 3$) mode are shown. In the spring-coupled cases, the mode shapes change continuously with the contact stiffness, Fig. 2.9 shows one example of normal contact stiffness and one of lateral contact stiffness. Other special cases of the characteristic equation (2.39) were published in literature [44, 60, 89]. The characteristic equation for a beam with normal and lateral springs at the end at $x = L$ was first published by Wright and Nishiguchi. [89].

The continuous change in mode shape as a function of contact stiffness is accompanied by a continuous change in resonant frequency. The lines labeled “A” in Fig. 2.10 show the resonant frequencies of the first four flexural modes as a function of normalized contact stiffness k^*/k_C for the clamped-spring-coupled beam (2.42). In this case the contact-resonance frequencies of the n 'th mode are always lower than the free resonant frequency of the subsequent mode ($n + 1$). The gaps in the spectrum between the clamped-pinned mode and the next clamped-free mode are shown as grey areas. If the sensor tip is moved away from the end of the beam ($L_2 > 0$), the maximum possible frequency shift increases. The case of a relative tip position $L_2/L = 5\%$ is shown as lines “B” in Fig. 2.10. If it happens for a mode that the distance of its last vibration node to the end of the beam becomes equal to or larger than the distance of the tip to the end, L_2 , this mode merges with the next higher mode and the situation becomes difficult to survey. As the wavelength decreases with increasing mode number, there are always higher modes for which this limit is surmounted. In the experiments it is therefore better to evaluate only modes for which the wavelength is greater than L_2 .

A torsional spring at the end of the beam (lines “C” in Fig. 2.10) also increases the shift of the resonant frequencies to higher values, such that the gaps in the spectrum disappear. The approximations for large n in Table 2.1 show that

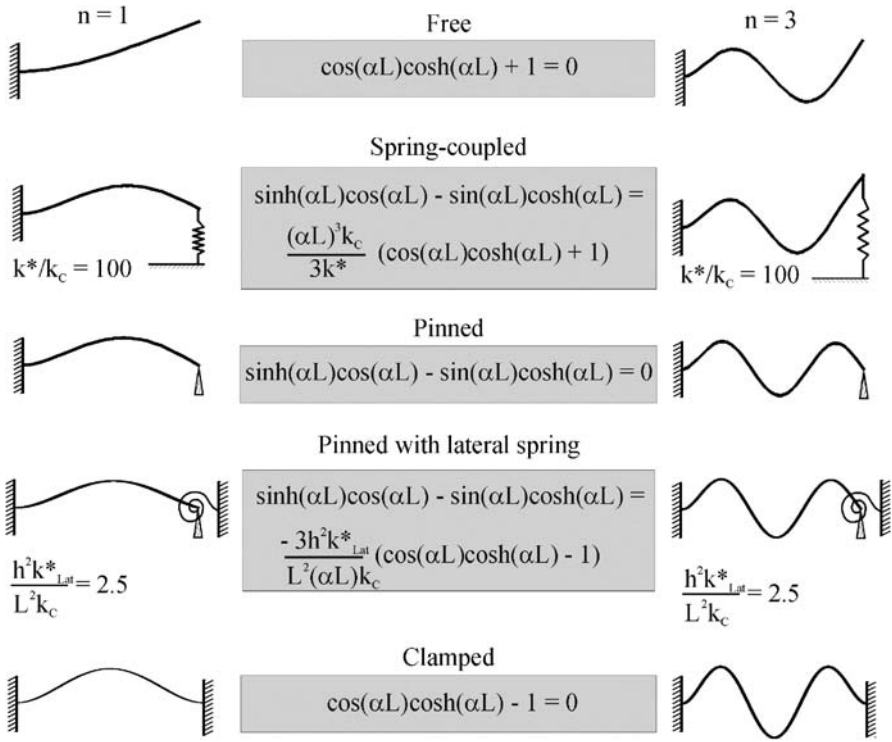


Fig. 2.9. Characteristic equations for some selected simple cases of the cantilever in flexural vibration. The shape functions $y(x)$ for the first flexural mode ($n = 1$) and the third mode ($n = 3$) are shown

the frequency of the $(n + 1)$ 'th clamped-free mode equals the frequency of the n 'th clamped-clamped mode. In a real experiment there will always be normal and lateral forces at the same time. However, even if the lateral contact stiffness is of the same size as the normal contact stiffness, its influence on the cantilever vibration is smaller than the influence of the normal stiffness, due to the factor h^2/L^2 which appears in the characteristic equation. The lateral forces are transformed into a moment by the lever-arm h of the sensor tip which is shorter than the cantilever length L . Typical sensor tip heights h are 5–15 μm , typical cantilever lengths L are 100–400 μm , i.e. h^2/L^2 ranges from 0.15 to 0.0125. As a consequence, the lateral contact stiffness influences the frequency little if the normal contact stiffness k^* is low compared to the spring constant of the cantilever k_c . At higher contact stiffness k^* the frequency shift comes closer to its upper limit, and the influence of the lateral contact stiffness k_{Lat}^* becomes remarkable. It was first pointed out by Mazeran and Loubet [25] that the influence of the lateral contact stiffness k_{Lat}^* is high when the ratio of the normal contact stiffness to the spring constant of the cantilever k^*/k_c is high. As a consequence, lateral forces may not be neglected if contact resonances are measured with soft sensor beams on stiff surfaces.

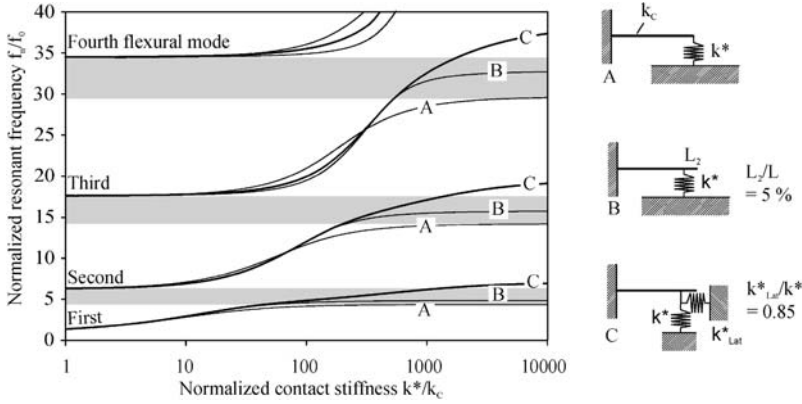


Fig. 2.10. Shift of the normalized resonant frequencies f_n/f_0 of the first four flexural modes as a function of normalized contact stiffness k^*/k_c . The lines labeled “A” show the case when only a spring normal to the sample surface is fixed to the cantilever. In case “B” the normal spring is fixed slightly away from the free end of the cantilever. In case “C” lateral tip-sample forces act additionally to the normal forces. A constant ratio between lateral and normal contact stiffness was assumed ($k_{Lat}^*/k^* = 0.85$)

Dupas et al. [60, 90] calculated the characteristic equation for the complete model shown in Fig. 2.8 with an additional spring at the clamped end of the cantilever. They examined the influence of the position and of the length of the sensor tip on the frequency shift of the first flexural mode. Arinero and L  v  que [26] calculated the contact vibrations of a beam with finite elements and examined the influence of the tip among other parameters. Wu et al. examined the influence of the length of the sensor tip on the frequency shift of the vibration modes [91].

2.4.2

Influence of an Additional Mass

An additional point-mass m_L on the cantilever shown schematically in Fig. 2.11 causes an inertial force proportional to $-\omega^2 m_L$. The influence of the mass can be found out easily if it is located at the tip position $x = L_1$ on the length axis of the beam [44, 92]. In this case the auxiliary function $U(\alpha)$ (2.38) in the boundary conditions (2.37) changes. If the center of gravity of the mass is displaced by ε from the middle plane of the beam, a moment proportional to $-\varepsilon^2 \omega^2 m_L$ [92] has to be added in the auxiliary function $T(\alpha)$. The form of the characteristic equation as well as the auxiliary function $X(\alpha)$ remain unchanged. With the help of the dispersion relation (2.6) one obtains:

$$\begin{aligned}
 T(\alpha) &= \frac{h^2}{L_1^3} (\phi(\alpha) \sin^2 \varphi + \phi_{Lat}(\alpha) \cos^2 \varphi) - \frac{\varepsilon^2 m_L}{L_1^3 m} (\alpha L_1)^4 \\
 U(\alpha) &= \frac{1}{L_1^3} (\phi(\alpha) \cos^2 \varphi + \phi_{Lat}(\alpha) \sin^2 \varphi) - \frac{1}{L_1^3} \frac{m_L}{m} (\alpha L_1)^4
 \end{aligned} \tag{2.44}$$

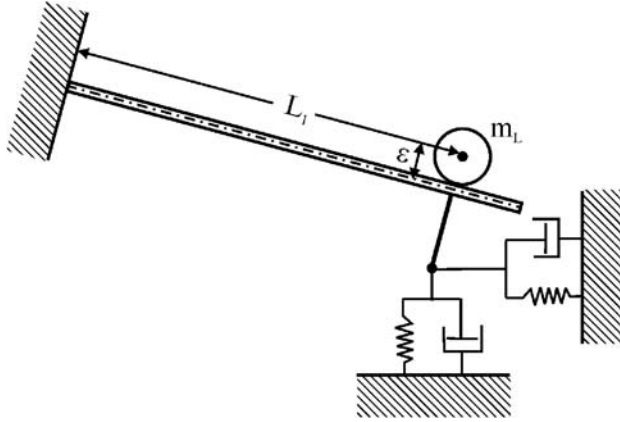


Fig. 2.11. An additional point mass m_L is located on the cantilever at $x = L_1$. The mass is displaced by ε from the middle plane of the beam indicated by the chain dotted line

It was assumed that $\rho A L_1 \approx m$, where m is the mass of the cantilever. This is a good approximation if the sensor tip is located close to the end of the beam. Without lateral forces, with a tip at the end of the beam ($L_2 = 0$), without tilt ($\varphi = 0$), and without damping one obtains the characteristic equation derived by Muraoka [92]:

$$3 \frac{k^*}{k_C} - \frac{m_L}{m} (\alpha L)^4 + \frac{(\alpha L)^3 [(1 + \cos \alpha L \cosh \alpha L) - \frac{\varepsilon^2}{L^2} \frac{m_L}{m} (\alpha L)^3]}{\sin \alpha L \cosh \alpha L + \sinh \alpha L \cos \alpha L} = 0 \quad (2.45)$$

$$- \frac{\varepsilon^2}{L^2} \frac{m_L}{m} (\alpha L)^3 (1 - \cos \alpha L \cosh \alpha L)$$

This equation was used to calculate the frequency shift in Fig. 2.12a. With increasing additional mass the cantilever behaves more and more like a point-mass oscillator. The frequency shift of the point-mass oscillator is according to (2.16):

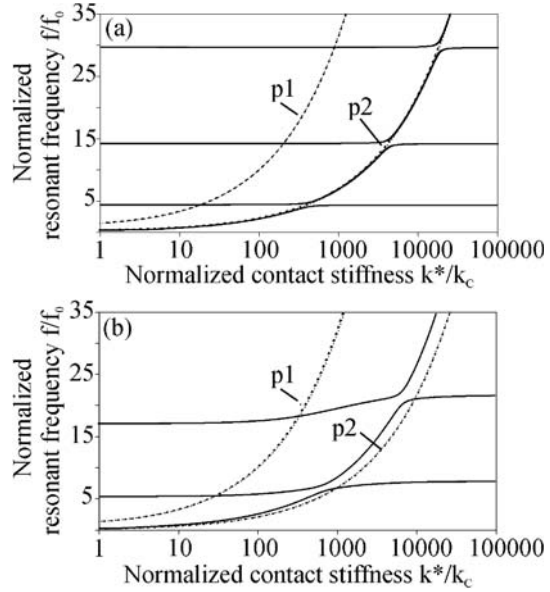
$$\frac{f}{f_0} = \sqrt{1 + \frac{k^*}{k_C}} \quad (2.46)$$

This behavior is shown in Fig. 2.12 as a dashed line (p1). In case of an additional mass at $x = L$ the point-mass model predicts the following frequency shift:

$$\frac{f}{f_0} = \sqrt{1 + \frac{k^*}{k_C}} \cdot \left(\sqrt{1 + 4 \frac{m_L}{m}} \right)^{-1} \quad (2.47)$$

An additional mass increases the effective mass of the beam and lowers its first free resonant frequency. The frequency shift according to the point-mass oscillator with additional mass (2.47) is labeled (p2) in Fig. 2.12. If the additional mass is high enough ($m_L/m = 5$) there are sections of the dispersion curves of the beam which coincide with the point-mass model. If contact-resonance frequencies are measured

Fig. 2.12. Influence of an additional mass m_L on the frequency shift of the contact-resonance frequencies (a) without lateral forces (displacement of the mass $\varepsilon = 0$, $m_L/m = 5$, position of the mass $L_1/L = 1$) [92], (b) with lateral forces (position $L_1/L = 0.9$, ratio of lateral contact stiffness to normal contact stiffness $k_{Lat}^*/k^* = 0.85$, beam angle $\varphi = 11^\circ$, cantilever length divided by tip height $L/h = 15$, mass displacement $\varepsilon = 0$, $m_L/m = 5$). The dashed lines show the frequency shift of the equivalent point-mass oscillator without additional mass (p1) and with additional mass m_L (p2)



and evaluated which lie on these sections, the simple point-mass formulas can be used to calculate the normalized contact stiffness k^*/k_C from the contact-resonance frequencies [92]. Muraoka observed an improved contrast when he used a cantilever with a W-particle glued onto its end for imaging in AFAM [93]. The characteristic equation with the additional mass can also be used to calculate the influence of the sensor tip on the vibration modes. For most commercial cantilevers, however, the influence of the mass of the tip is negligible.

2.4.3

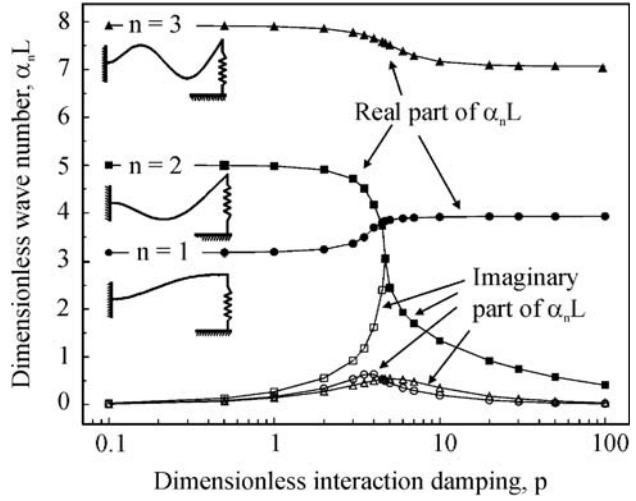
Roots of the Characteristic Equation with Damping

In the discussion of the characteristic equation the influence of the contact damping has not been considered so far. In a simplified case without lateral forces and tilt of the beam, the characteristic equation becomes [70]:

$$(\alpha L)^3 (1 + \cos \alpha L \cosh \alpha L) + \left(3 \frac{k^*}{k_C} + i(\alpha L)^2 p \right) \times (\sin \alpha L \cosh \alpha L - \sinh \alpha L \cos \alpha L) = 0 \quad (2.48)$$

The solutions $\alpha_n L$ of this equation are complex numbers. The influence of the contact damping on the real part and the complex part of the wave number is shown in Fig. 2.13 [70]. The shapes of the first three modes in the case of a ratio of the normal contact stiffness to the spring constant of the cantilever $k^*/k_C = 10$ and without contact damping ($p = 0$) are shown as insets. With increasing contact damping p mode 1 shows stiffening behavior, i.e. the frequency increases, while

Fig. 2.13. Influence of the dimensionless contact damping p on the first three modes in the case $k^*/k_C = 10$. The real part (filled symbols) and the imaginary part (open symbols) of the eigenvalues $\alpha_n L$ are plotted as a function of p



mode 2 shows softening behavior. Both modes have a maximum of the imaginary part of the wave number in the frequency interval where the real part of $\alpha_n L$ changes strongly. Note that the horizontal scale in Fig. 2.13 is logarithmic. The stiffness of mode 2 decreases strongly, the imaginary part of $\alpha_n L$ increases at first, then it decreases again and in this part of the curve the absolute values of the real and the imaginary parts are identical. A closer experimental and theoretical study of how the vibration modes behave as a function of interaction damping could lead to new techniques to measure tip-sample interaction damping or even internal friction at sample surfaces.

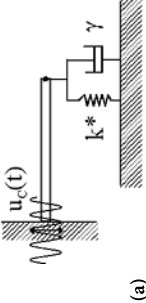
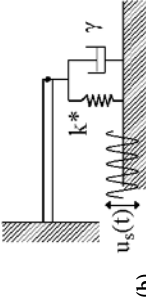
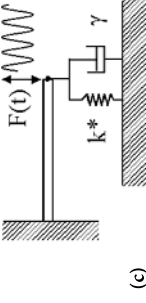
2.5

Forced Vibration

Three types of excitation shown in Table 2.3 play an important role in AFM. (a) It is possible to vibrate the clamped end of the cantilever harmonically in its thickness direction with an amplitude $u_c(t) = u_0 e^{i\omega t}$ (UAFM). (b) The sample surface is set into normal vibration with an amplitude $u_s(t) = u_0 e^{i\omega t}$ (AFAM). (c) A concentrated harmonic force $F(t) = F_0 e^{i\omega t}$ – for example a magnetic force – acts directly on the cantilever. The excitation signal is added to the boundary conditions. Afterwards the general solution and its derivatives are substituted in the boundary conditions and the constants A_1 , A_2 , A_3 and A_4 are calculated as a function of excitation frequency. Table 2.3 shows a simplified situation with only a spring and a damper at the end of the beam. The boundary conditions are in the AFAM mode, case (b):

$$x = 0 : \begin{cases} y = a_0 \\ \frac{\partial y}{\partial x} = 0 \end{cases} \quad x = L : \begin{cases} \frac{\partial^2 y}{\partial x^2} = 0 \\ \frac{\partial^3 y}{\partial x^3} = \frac{\phi(\alpha)}{L^3} (y - u_0) \end{cases} \quad (2.49)$$

Table 2.3. Boundary conditions and solutions for the forced flexural vibration of a cantilever beam. Three techniques of excitation are treated: (a) Vibration of the clamped end of the cantilever, (b) sample surface vibration, (c) modulated concentrated force acting at $x = L$

 <p>(a)</p>	 <p>(b)</p>	 <p>(c)</p>
Fixed end: $u_c(t) = u_0 e^{i\omega t}$	Sample surface: $u_s(t) = u_0 e^{i\omega t}$	Force at $x = L$: $F(t) = F_0 e^{i\omega t}$
$x=0: \begin{cases} y = u_0 \\ \frac{\partial y}{\partial x} = 0 \\ \frac{\partial^3 y}{\partial x^3} = \frac{\phi(\alpha)}{L^3} y \end{cases} \quad \begin{cases} \frac{\partial^2 y}{\partial x^2} = 0 \\ x = L: \\ \frac{\partial^3 y}{\partial x^3} = \frac{\phi(\alpha)}{L^3} y \end{cases}$	$x=0: \begin{cases} y = a_0 \\ \frac{\partial y}{\partial x} = 0 \\ \frac{\partial^3 y}{\partial x^3} = \frac{\phi(\alpha)}{L^3} (y - u_0) \end{cases} \quad \begin{cases} \frac{\partial^2 y}{\partial x^2} = 0 \\ x = L: \\ \frac{\partial^3 y}{\partial x^3} = \frac{\phi(\alpha)}{L^3} y \end{cases}$	$x=0: \begin{cases} y = 0 \\ \frac{\partial y}{\partial x} = 0 \\ \frac{\partial^3 y}{\partial x^3} = \frac{\phi(\alpha)}{L^3} y - \frac{F_0}{EI} \end{cases} \quad \begin{cases} \frac{\partial^2 y}{\partial x^2} = 0 \\ x = L: \\ \frac{\partial^3 y}{\partial x^3} = \frac{\phi(\alpha)}{L^3} y - \frac{F_0}{EI} \end{cases}$
$y(x) = \frac{u_0}{2} (\cos \alpha x + \cosh \alpha x) + A_2 (\cos \alpha x - \cosh \alpha x) + A_4 (\sin \alpha x - \sinh \alpha x)$	$y(x) = A_2 (\cos \alpha x - \cosh \alpha x) + A_4 (\sin \alpha x - \sinh \alpha x)$	$y(x) = A_2 (\cos \alpha x - \cosh \alpha x) + A_4 (\sin \alpha x - \sinh \alpha x)$
$A_2 = \frac{u_0}{2} \frac{\phi(\alpha) \text{mix}^+ - (\alpha L)^3 \sin \alpha L \sinh \alpha L}{N(\alpha)}$	$A_2 = -\frac{u_0}{2} \frac{\phi(\alpha) (\sin \alpha L + \sinh \alpha L)}{N(\alpha)}$	$A_2 = -\frac{F_0 L^3}{2EI} \frac{\sin \alpha L + \sinh \alpha L}{N(\alpha)}$
$A_4 = \frac{u_0}{2} \frac{-2\phi(\alpha) \cos \alpha L \cosh \alpha L + (\alpha L)^3 m^+}{N(\alpha)}$	$A_4 = \frac{u_0}{2} \frac{\phi(\alpha) (\cos \alpha L + \cosh \alpha L)}{N(\alpha)}$	$A_4 = \frac{F_0 L^3}{2EI} \frac{\cos \alpha L + \cosh \alpha L}{N(\alpha)}$
$y(L) = u_0 (\alpha L)^3 \frac{\cos \alpha L + \cosh \alpha L}{N(\alpha)}$ $\frac{\partial y}{\partial x} \Big _{x=L} = \alpha u_0 \frac{(\alpha L)^3 s^- + \phi(\alpha) c^-}{N(\alpha)}$	$y(L) = u_0 \phi(\alpha) \frac{\sin \alpha L \cosh \alpha L - \sinh \alpha L \cos \alpha L}{N(\alpha)}$ $\frac{\partial y}{\partial x} \Big _{x=L} = \alpha u_0 \phi(\alpha) \frac{\sin \alpha L \sinh \alpha L}{N(\alpha)}$	$y(L) = \frac{3F_0}{k_C} \frac{\sin \alpha L \cosh \alpha L - \sinh \alpha L \cos \alpha L}{N(\alpha)}$ $\frac{\partial y}{\partial x} \Big _{x=L} = \alpha \frac{3F_0}{k_C} \frac{\sin \alpha L \sinh \alpha L}{N(\alpha)}$
$\text{mix}^+ \equiv \sin \alpha L \cosh \alpha L + \sinh \alpha L \cos \alpha L, \quad s^- \equiv \sin \alpha L - \sinh \alpha L, \quad c^- \equiv \cos \alpha L - \sinh \alpha L$		

From the first two boundary conditions one obtains $A_1 = A_3 = 0$, and with the third boundary condition the shape function becomes:

$$y(x) = A_2(\cos \alpha x - \cosh \alpha x) + A_4(\sin \alpha x - \sinh \alpha x) \quad (2.50)$$

From the last boundary condition the constants A_2 and A_4 are calculated:

$$A_2 = -\frac{u_0 \phi(\alpha)}{2N(\alpha)}(\sin \alpha L + \sinh \alpha L) \quad A_4 = \frac{u_0 \phi(\alpha)}{2N(\alpha)}(\cos \alpha L + \cosh \alpha L) \quad (2.51)$$

The denominator of the two constants in the foregoing equations is the same:

$$N(\alpha) = (\alpha L)^3(1 + \cos \alpha L \cosh \alpha L) + \phi(\alpha)(\cosh \alpha L \sin \alpha L - \sinh \alpha L \cos \alpha L) \quad (2.52)$$

The complex amplitude of vibration is obtained by substituting (2.51) and (2.52) in (2.50):

$$y(x) = \frac{u_0 \phi(\alpha)}{2N(\alpha)} [-(\sin \alpha L + \sinh \alpha L)(\cos \alpha x - \cosh \alpha x) + (\cos \alpha L + \cosh \alpha L)(\sin \alpha x - \sinh \alpha x)] \quad (2.53)$$

The detector, for example the laser spot of an interferometer, is usually located at the end of the beam. In this case one only needs the amplitude at $x = L$, and (2.53) simplifies to:

$$y(L) = u_0 \frac{\sin \alpha L \cosh \alpha L - \sinh \alpha L \cos \alpha L}{N(\alpha)} \quad (2.54)$$

Commercial atomic force microscopes are generally equipped with beam-deflection sensors. Their signal is proportional to the angle of the cantilever, given by the derivative of $y(x)$. At the end of the beam at $x = L$ the derivative is:

$$\left. \frac{\partial y}{\partial x} \right|_{x=L} = \frac{\alpha L u_0}{L} \frac{\sin(\alpha L) \sinh(\alpha L)}{N(\alpha)} \quad (2.55)$$

The boundary conditions and shape functions for the three mentioned cases of excitation are shown in Table 2.3. The amplitudes and slopes in (2.54) and in (2.55) are complex numbers. Real amplitude and phase Φ of the signals are calculated here using:

$$|y(x)| = \sqrt{\text{Im}[y(x)]^2 + \text{Re}[y(x)]^2} \quad \Phi(x) = -\arctan \frac{\text{Im}[y(x)]}{\text{Re}[y(x)]} \quad (2.56)$$

The normalized vertical amplitude of the sensor tip d_{y0} and the normalized lateral amplitude d_{x0} of the sensor tip are defined according to:

$$d_{y0} = |y(L)| / u_0 \quad d_{x0} = h \left| \frac{\partial y}{\partial x}(L) \right| / u_0 \quad (2.57)$$

The lateral amplitude is the amplitude in x -direction, parallel to the length axis of the cantilever. Note that the vertical and lateral amplitudes d_{y0} and d_{x0} , respectively, are only normal and lateral to the sample surface if the cantilever is not tilted ($\varphi = 0$).

Figure 2.14 shows examples of forced vibration calculated with the formulas in Table 2.3 (a) and (b). The normalized vibration amplitude d_{y0} and the normalized lateral vibration amplitude d_{x0} are shown for three different values of normalized contact stiffness k^*/k_c . The lateral amplitude, which is proportional to the beam-deflection signal, becomes very small in the case $k^*/k_c = 10$ for the first mode and very high in the case $k^*/k_c = 100$. The maxima are marked as (1) and (2) in Fig. 2.14(c) and (d). Figure 2.15 shows the corresponding mode shapes $y(x)$. The shape of the first mode is similar to the shape of a pinned mode in the case $k^*/k_c = 100$. This leads to high lateral amplitude at the end of the beam and a strong beam-deflection signal. In the case $k^*/k_c = 10$ the lateral deflection becomes almost zero at the end of the beam, and the first mode is hardly visible if a beam-deflection sensor is used and if the laser spot is focused to the end of the beam. The beam-deflection detector is most sensitive when the laser spot is located in one of the nodes of the vibration mode. The first mode will therefore be detectable if the

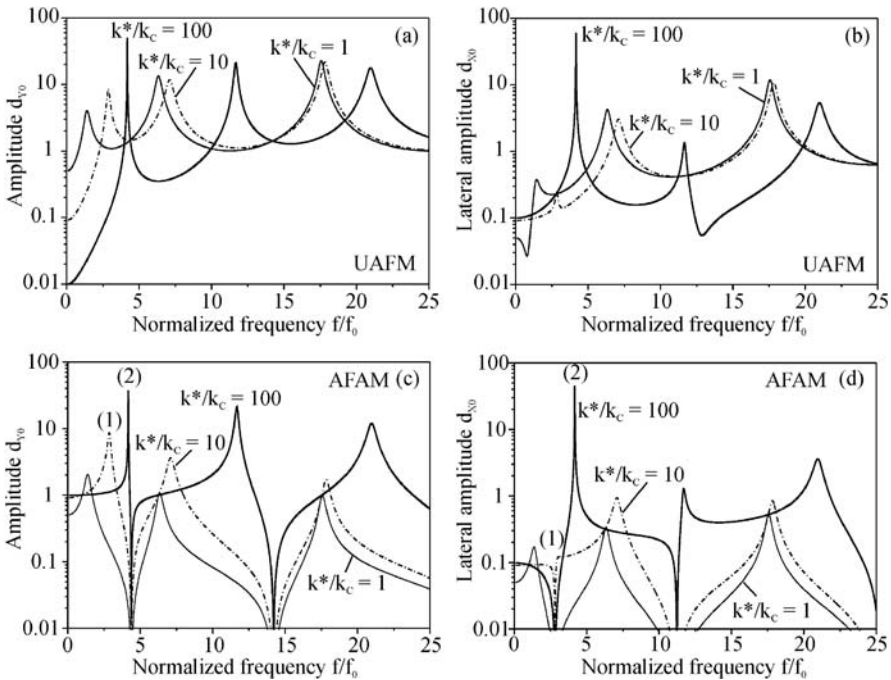


Fig. 2.14. Forced vibration of a cantilever calculated with the formulas shown in Table 2.3 for excitation at the clamped end and excitation by the sample surface. The vertical and lateral amplitudes of the sensor tip d_{y0} and d_{x0} , respectively, are shown for three different values of contact stiffness. In Figs. (a) and (b) the vibration was excited at the clamped end (UAFM) and in Figs. (c) and (d) the vibration was excited by sample surface vibration (AFAM). The damping constants used for the calculation were $Q_{1,\text{free}} = 300$ and $\gamma/(m^*\omega_0) = 0.4$

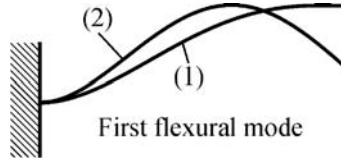


Fig. 2.15. Shape functions $y(x)$ of the modes corresponding to the peaks marked as (1) and (2) in Figs. 5.1 (c) and (d). The spring and the dashpot representing the contact forces are not shown here

laser spot is moved towards the middle of the beam. However, this decreases the sensitivity of the detection system to static forces and there is the risk that a position more in the middle of the beam corresponds to an antinode of one of the higher modes.

All solutions in Table 2.3 have the same denominator $N(\alpha)$. The denominator contains the characteristic equation (here the characteristic equation of the simplified case without tilt of the cantilever and without lateral forces). In the case of low damping the zeros of the denominator are the resonant frequencies of the system, and the resonant frequencies are independent of the method of vibration excitation, as can be seen in Fig. 2.16. The measured amplitudes, however, depend strongly on the type of excitation, on the method of detection (amplitude or slope) and on the position of the detecting laser spot on the length axis of the cantilever. In the AFAM-mode one observes anti-resonances between the resonant frequencies where

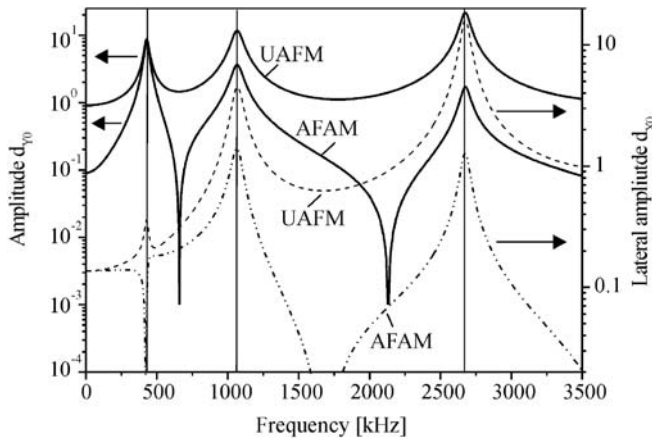


Fig. 2.16. Vertical amplitude d_{y0} and lateral amplitude d_{x0} in the UAFM and AFAM mode. The case of a normalized contact stiffness of $k^*/k_C = 10$ was chosen. A measurement at the end of the beam was assumed ($x = L$). The vertical lines show that the detected resonant frequencies are independent of the type of excitation and also independent of whether one detects the amplitude of the beam (equal to the vertical tip amplitude) or the slope of the beam (proportional to the lateral tip amplitude) if the damping is low. The constants used for the simulation were: Resonant frequency of the clamped-free beam $f_{1,\text{free}} = 150$ kHz, $Q_{1,\text{free}} = 300$, contact damping $\gamma/(m^*\omega_0) = 0.4$

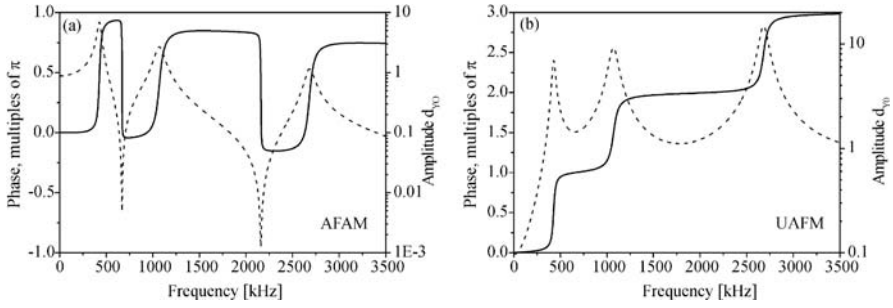


Fig. 2.17. Amplitude (*dashed line*) and phase (*continuous line*) in the AFAM-mode (a) and in the UAFM-mode (b). In the AFAM-mode (a) anti-resonances accompanied by a phase shift of $-\pi$ are observed. The data for the calculation were the same as in Fig. 2.16

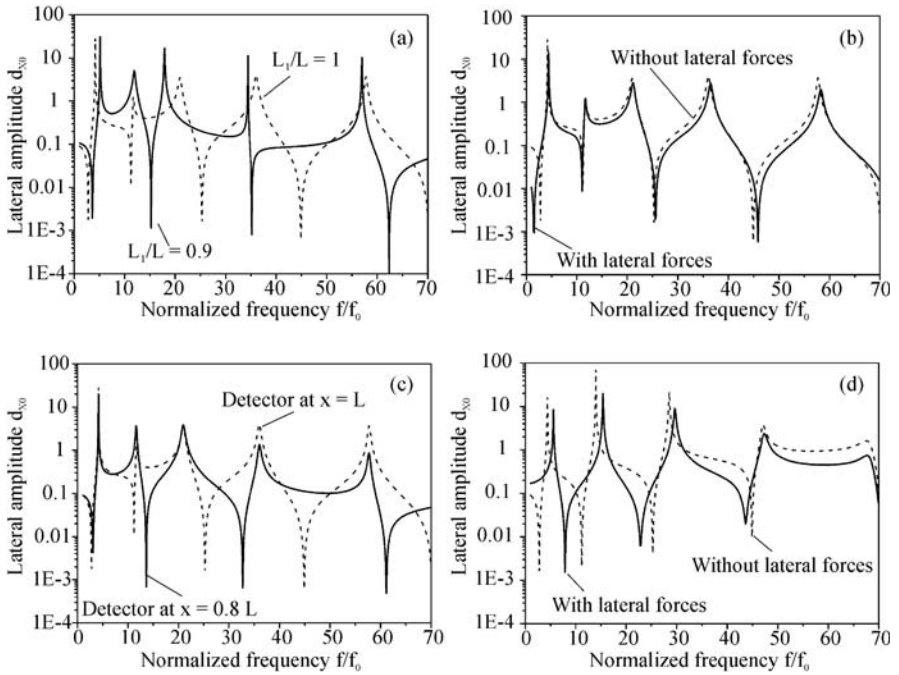


Fig. 2.18. Forced vibration in the AFAM-mode. The lateral amplitude d_{y0} is shown. This signal is proportional to the beam-deflection signal. (a) Influence of the position of the sensor tip (b), influence of the lateral forces in the case of normalized contact stiffness $k^*/k_C = 100$, contact damping $\gamma/(m^*\omega_0) = 0.4$. (c) Influence of the position of the laser spot on the detected signal, (d) influence of the lateral forces in the case $k^*/k_C = 1000$, $\gamma/(m^*\omega_0) = 2$. For the lateral forces in (b) and (d) a ratio of lateral to normal contact function $\phi_{Lat}(\alpha)/\phi(\alpha) = 0.85$, an angle $\varphi = 11^\circ$, and a ratio cantilever-length to tip-height of $L/h = 15$ was assumed

the amplitude becomes zero and the phase shifts by $-\pi$ (Fig. 2.17). This holds also for the slope of the cantilever (not shown here).

The solutions for the forced vibration of the complete system according to Fig. 2.8 including lateral forces and tip position can be found in the appendix. A few examples of forced vibration are plotted in Fig. 2.18. The tip position influences the resonant frequencies strongly in all cases, as can be seen in Fig. 2.18a. A shift of the tip from the end position ($L_1/L = 1$) to a position only 10% of the length of the beam closer to the fixed end ($L_1/L = 0.9$) leads to a dramatic change in the spectrum. The lateral forces influence the spectrum less when the normal contact stiffness divided by the spring constant of the cantilever is lower ($k^*/k_C = 100$) (b), and they influence the spectrum more when the normal contact stiffness is high ($k^*/k_C = 1000$) (d). The detector position influences the amplitudes of the measured peaks (c). The first mode, which is not well visible with the beam-deflection sensor at the end of the beam, is much better visible if the detector is located at $x = 0.8L$. The resonance frequencies do not depend on the detector position, but the frequencies of the anti-resonances depend strongly on the position of the detector on the length axis of the beam. This was also pointed out by Arinero and L  v  que [26].

2.6

Imaging and Contrast Inversion

There are different possibilities to evaluate the contact resonances for imaging, as for example amplitude or phase imaging. The cantilever-sample system is excited with a frequency close to a contact resonance [62]. The contact-resonance frequency must be higher than the upper cut-off of the feedback loop. The feedback loop of the AFM works with the quasi static and low frequency components of the cantilever signal and keeps the static deflection of the cantilever at a predefined value while the surface is scanned. Parallel to the topography image the ultrasonic amplitude or phase is measured for example with a lock-in-amplifier and displayed as a color coded image. An example of a topography image and an ultrasonic amplitude image of a piezoelectric ceramic is shown in Fig. 2.19. In the topography image the grains of the polished sample surface can be seen. In the ultrasonic image substructures are visible within the grains which are the ferroelectric domains. The contact stiffness in AFAM and UAFM depends on the orientation of the domains [83, 94].

The contrast of the amplitude images depends strongly on the frequency of operation [95, 96] as shown in Fig. 2.20. If the frequency of operation is far from any contact resonance, the contrast vanishes. If the frequency of excitation is lower than the average contact-resonance frequency of the sample, regions with high stiffness will cause lower amplitude of vibration than regions with low stiffness. And if the frequency is higher than the average contact-resonance frequency the contrast inverts. Experimental observation of contrast inversion is an indicator for a contact-resonance frequency. It is recommended to operate above the contact-resonance frequency if possible, because the images are more intuitive if surface areas with higher stiffness show higher amplitude of vibration.

Imaging of samples with a high variation of Young's modulus as for example polymer samples with ceramic inclusions will lead to a shift of the contact-resonance

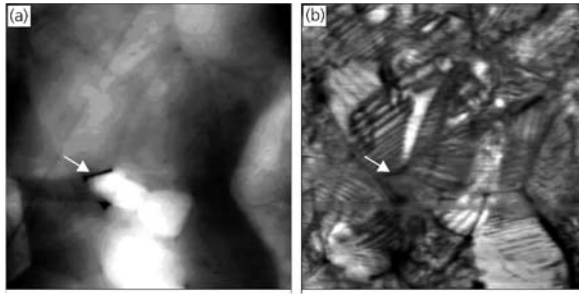


Fig. 2.19. Topography-image (a) and AFAM amplitude-image (b) of a piezoelectric ceramic [82]. The size of the image is $10 \times 10 \mu\text{m}^2$. The grey scale in the topography image covers 20 nm. The spring constant of the cantilever was 41 N/m. The first two flexural resonant frequencies of the clamped-free beam were 162 kHz and 1004 kHz. The ultrasonic amplitude image was taken above the first contact-resonance frequency at 698 kHz. The *white arrows* point to a pore in the ceramic surface

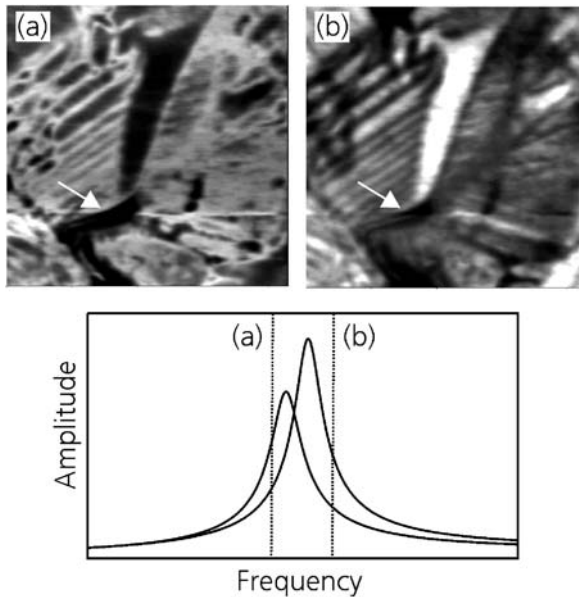


Fig. 2.20. Contrast inversion depending on the ultrasonic excitation frequency [95]. A smaller section of the same surface as in Fig. 2.19 was imaged (a) at a frequency below the contact-resonance frequency (695 kHz) and (b) above the contact-resonance frequency (699 kHz). The large triangular domain in the middle of the image changes contrast when the frequency of imaging is changed. The principle of contrast inversion is explained in the simulated spectra below. Areas with higher contact stiffness lead to a higher contact-resonance frequency. The *dotted lines* indicate schematically the frequency of operation below and above the average resonant frequency. The *white arrows* point to the same pore as seen in Fig. 2.19. The ultrasonic amplitude is always low and contrast inversion is not observed when the tip is on the pore. The topography of the pore leads to a strong variation of contact stiffness and consequently to a contact-resonance frequency much different from the flat areas of the sample

frequency within one image amounting to several multiples of the half-width of the resonant peaks. In this case it is no more possible to find a frequency which is close to the contact-resonance maximum on both phases. Several contrast inversions may happen within one image and the qualitative correspondence between amplitude and stiffness is lost. Strong variations of contact stiffness are also caused by topographical features. One such example can be seen in Fig. 2.20. If the tip is above the small pore in the ceramic which is indicated by white arrows in Fig. 2.19 and Fig. 2.20, the amplitude of vibration is low in both cases of excitation frequency. Probably, the contact-resonance frequency of this area is much different from the contact-resonance frequency of the flat surface regions.

The contrast in the amplitude images is caused by the shift of the contact-resonance frequency with contact stiffness. Furthermore, the amplitude at contact resonance varies with contact stiffness. The theoretical amplitudes at contact resonance of the first three modes are shown in Fig. 2.21.

Amplitude or phase imaging is a convenient method to obtain qualitative images of contact-stiffness variation. For quantitative evaluation, however, it is necessary to measure the contact-resonance frequency in every pixel of the image. Kobayashi

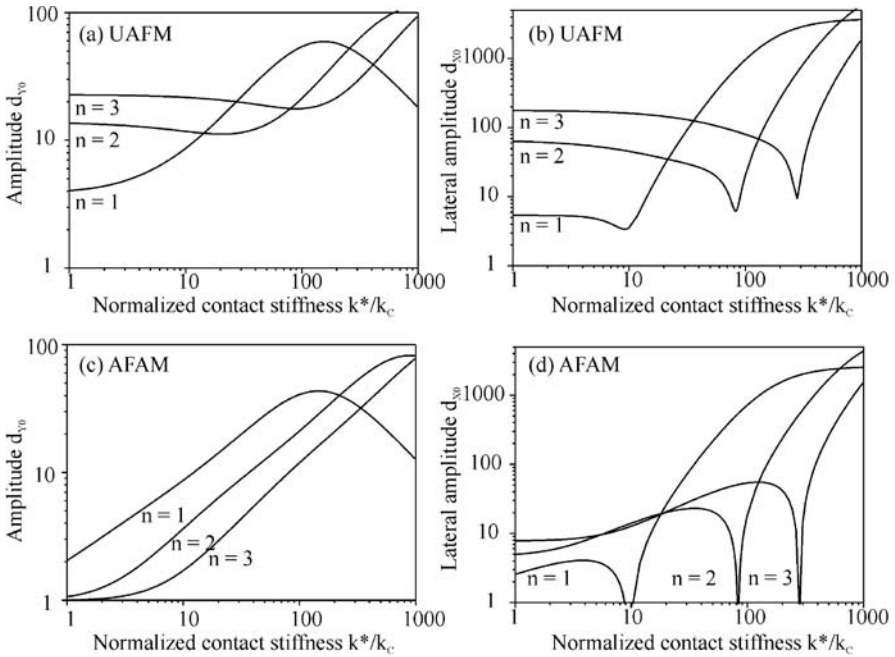


Fig. 2.21. Vertical amplitude of the sensor tip d_{y0} and lateral amplitude d_{x0} at the contact-resonance frequency of the first three flexural modes as a function of normalized contact stiffness. A detector position at the end of the beam ($x = L$) was assumed and a low contact damping ($\gamma/(m^*\omega_0) = 0.4$) was used for the calculation. The curves were obtained by taking the amplitude maxima of simulated contact-resonance curves. All modes have local minima in the lateral amplitude for contact stiffness values at which the slope of the shape function $y(x)$ has local minima at $x = L$

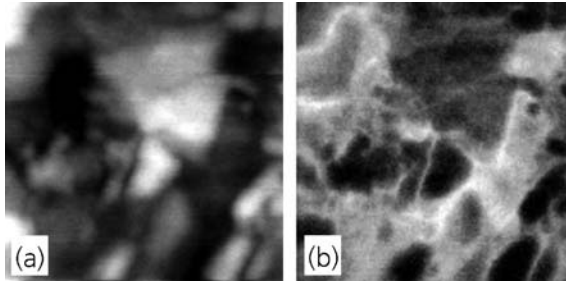


Fig. 2.22. Topography, height scale 10 nm (a) and contact resonance AFAM-image (b) of nanocrystalline nickel with an average grain size of 167 nm fabricated by pulsed electrodeposition. The sample was polished with diamond paste and alumina solution before imaging [119]. The grey scale of the contact-resonance image ranges from 730 kHz to 750 kHz. The size of the images is $1.5 \times 1.5 \mu\text{m}^2$

et al. developed a phased-locked-loop for the UAFM in order to follow the contact-resonance frequency during imaging [97]. The technique was enhanced by amplitude detection by Yamanaka et al. [98]. Fukuda et al. showed that the Q -control technique [99] which was originally developed for tapping mode AFM can also be applied in UAFM [100]. Fast computers and high storage capacities make it possible to sweep spectra in every image point to track the contact-resonance frequency [101, 102] or to save full vibration spectra in every image point (Solver and Ntegra, NT-MDT, Moscow, Russia). The velocity of imaging is only limited by the frequency of vibration and by the contact damping. If contact resonances between 100 kHz and 1 MHz are measured, an image of 128×128 pixels takes about half an hour. Topography and contact-resonance frequency images of a nanocrystalline nickel sample are shown in Fig. 2.22. The sample was polished before imaging. The average grain size of the material was 167 nm.

2.7

Sensitivity of the Flexural Modes

The influence of the forces which act upon the sensor tip is different for different modes because the mode shape and the wavelength depend on the mode number. In case of quantitative evaluation, the frequency shift of the contact resonances is relevant. The derivative $\partial f / \partial k^*$ was calculated analytically by Turner and Wiehn [65]. Normalized quantities marked with the symbol “ \wedge ” are used here to shorten the calculations:

$$\hat{k} = \frac{k^*}{k_c}, \quad \hat{k}_{\text{Lat}} = \frac{k_{\text{Lat}}^*}{k_c}, \quad \hat{f} = \frac{f}{f_{1,\text{free}}}, \quad (2.58)$$

and abbreviations for combinations of the trigonometric and hyperbolic functions which appear frequently are introduced:

$$\begin{aligned}
ssh(x) &= \sin(x) \sinh(x) \\
cch(x) &= \cos(x) \cosh(x) \\
cch^\pm(x) &= 1 \pm \cos(x) \cosh(x) \\
mix^\pm(x) &= \sin(x) \cosh(x) \pm \cos(x) \sinh(x)
\end{aligned} \tag{2.59}$$

The dimensionless wave number ψ is defined as $\psi = \alpha L$. The characteristic equation is a function of the wave number, the contact stiffness and the contact damping. The characteristic equation (2.39) is rewritten in normalized quantities, and only the dependency on the normalized contact stiffness \hat{k}^* is considered:

$$\Omega(\psi(\hat{k}^*), \hat{k}^*) = 0 \tag{2.60}$$

The derivative of this equation with respect to \hat{k}^* yields [65]:

$$\frac{d\psi}{d\hat{k}^*} = -\frac{\partial\Omega}{\partial\hat{k}^*} \left(\frac{\partial\Omega}{\partial\psi} \right)^{-1} \tag{2.61}$$

If this formula is applied for example to the characteristic equation of the spring-coupled cantilever (2.42) one obtains:

$$\frac{d\psi}{d\hat{k}^*} = \frac{-3mix^-(\psi)}{3\psi^2cch^+(\psi) - \psi^3mix^-(\psi) + 6\hat{k}^*ssh(\psi)} \tag{2.62}$$

As the sensitivity is given by the shift of the resonant frequency and not by the shift of the dimensionless wave number, the chain rule and the dispersion relation (2.10) are used:

$$\frac{\partial\hat{f}}{\partial\hat{k}^*} = \frac{\partial\hat{f}}{\partial\psi} \frac{\partial\psi}{\partial\hat{k}^*} \quad \frac{\partial\hat{f}}{\partial\psi} = 2 \frac{\psi}{(1.8751)^2} \tag{2.63}$$

Now, the sensitivity σ can be calculated:

$$\sigma = \frac{d\hat{f}}{d\hat{k}^*} = \frac{-6\psi mix^-(\psi)}{(1.8751)^2 [3\psi^2cch^+(\psi) - \psi^3mix^-(\psi) + 6\hat{k}^*ssh(\psi)]} \tag{2.64}$$

To evaluate the sensitivity, the normalized wave number or the contact-resonance frequency is first determined using the characteristic equation (2.42). Afterwards, (2.64) is applied. The sensitivity of the first four flexural modes of the spring-coupled cantilever is shown in Fig. 2.23. In the limit of vanishing contact stiffness ($\hat{k}^* = 0$) the normalized wave number is $\psi = 1.8751$ and $cch^+(1.8751) = 0$. Therefore the sensitivity of the first flexural mode is in the limit $\hat{k}^* = 0$:

$$n = 1 : \sigma(\hat{k}^* = 0) = \left. \frac{d\hat{f}}{d\hat{k}^*} \right|_{\hat{k}^*=0} = \frac{6}{(1.8761)^4} \approx 0.5 \tag{2.65}$$

In general one obtains for the n 'th mode in the limit $\hat{k}^* = 0$:

$$\left. \frac{d\hat{f}}{d\hat{k}^*} \right|_{k^*=0} = \frac{6}{(1.8761)^2 (\psi_{n,\text{free}})^2} \quad (2.66)$$

For each value of the contact stiffness one can determine a flexural mode with highest sensitivity. The approximate crossing points of the sensitivity curves in Fig. 2.23 are listed in Table 2.4. The higher the contact stiffness, the higher is the most sensitive mode. The acoustic impedance at the sensor-tip position increases with the mode number [70]. One can also say that the dynamic load which is imposed by the cantilever onto the sample increases with increasing frequency proportional $m^* \omega^2 y(L)$ [27, 29]. However, the maximal value of the sensitivity $\sigma \approx 0.5$ is only reached by the first mode for small contact stiffness ($k^* \rightarrow 0$). This means that the sensitivity can be improved by using higher modes, but the sensitivity of the higher modes of a soft beam will be smaller than the sensitivity of the first mode

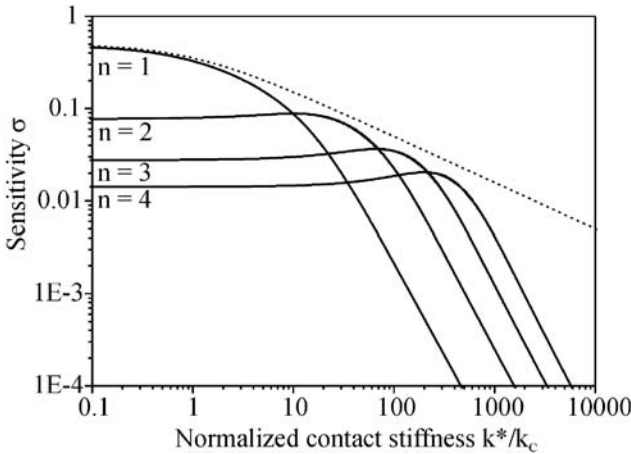


Fig. 2.23. Sensitivity σ of the first four flexural modes as a function of normalized contact stiffness [65]. The dashed line shows the sensitivity according to the equivalent point-mass model

Table 2.4. Linear model of the cantilever when the sensor tip is in contact with a sample surface. The tip-sample interaction forces are represented by springs and dashpots. The cantilever is tilted by an angle φ with respect to the surface. The sensor tip of height h is located at a position L_1 on the length axis of the cantilever. The distance of the tip to the free end of the cantilever is L_2

Mode number n	1	2	3
Slope at $x = L$ becomes zero	$k^*/k_C = 9.5$	$k^*/k_C = 83$	$k^*/k_C = 279$
Mode $(n + 1)$ becomes more sensitive than mode n	$k^*/k_C \approx 9.9$	$k^*/k_C \approx 69$	$k^*/k_C \approx 216$
	$\sigma \approx 0.09$	$\sigma \approx 0.04$	$\sigma \approx 0.02$
Sensitivity of n 'th flexural mode for $k^* \rightarrow 0$	$\sigma = 0.485$	$\sigma = 0.077$	$\sigma = 0.028$

of a stiffer beam. Unfortunately, a stiffer beam makes the control of the static force more difficult. As the static force is also an important parameter, the choice of the optimal cantilever is always a compromise.

Using the Rayleigh–Ritz method, Turner and Wiehn calculated an approximate formula for the sensitivity of the first five flexural and torsional modes [65]. This solution can also be applied to cantilevers with variable cross-section as for example V-shaped beams. The analytical formula of Turner and Wiehn was extended to contact damping by Chang et al. [103]. They found that the contact damping reduces the sensitivity of the modes for small values of contact stiffness k^* . Furthermore the influence of lateral forces and tilt [104] and the length of the sensor tip [91] were examined. As the contact stiffness depends on the radius of the sensor tip and the Young’s moduli of tip and surface, it is not possible to calculate general formulas for the sensitivity as a function of Young’s modulus of the sample. For such a calculation one must assume a certain tip radius, elastic modulus and static force [96].

2.8

Quantitative Evaluation

The characteristic equation derived in Chap. 4 can be solved for an analytical expression which describes the normalized contact stiffness k^*/k_C as a function of contact resonance. The ratio c_P between lateral and normal contact function is defined as:

$$c_P = \frac{\phi_{\text{Lat}}(\alpha)}{\phi(\alpha)} \quad (2.67)$$

Substituting the auxiliary functions X , T , U (2.38) in the characteristic equation (2.39, 2.40), one obtains a quadratic equation in the contact function $\phi(\alpha)$:

$$\begin{aligned} L_1^4 S_4 + L_1^3 S_3 \frac{h^2}{L_1^2} \phi(\alpha) [\sin^2 \varphi + c_P \cos^2 \varphi] + L_1^2 S_2 \frac{h}{L_1} \phi(\alpha) \sin \varphi \cos \varphi [c_P - 1] \\ + L_1 S_1 \phi(\alpha) [\cos^2 \varphi + c_P \sin^2 \varphi] + S_0 \frac{h^2}{L_1^2} \phi^2(\alpha) c_P = 0 \end{aligned} \quad (2.68)$$

The quadratic term in $\phi(\alpha)$ vanishes if there are no lateral forces ($c_P = 0$). If the cantilever is parallel to the sample surface ($\varphi = 0$), one obtains the following solution for the contact function $\phi(\alpha)$:

$$\phi(\alpha) = -\frac{L_1^4 S_4}{L_1 S_1} = \frac{2(\alpha L_1)^3 cch^+(\alpha L)}{cch^-(\alpha L_1)mix^-(\alpha L_2) - cch^+(\alpha L_2)mix^-(\alpha L_1)} \quad (2.69)$$

In the experiment a contact-resonance frequency f_{Cont} is measured. If the resonant frequencies of the free cantilever are known, the dispersion relation (2.10) containing the measurable quantities can be used to calculate the wave numbers from the measured contact-resonance frequencies:

$$\alpha L = \frac{\alpha_{n,\text{free}} L}{\sqrt{f_{n,\text{free}}}} \sqrt{f_{\text{Cont}}} = c_n \sqrt{f_{\text{Cont}}} \quad \text{with} \quad c_n := \frac{\alpha_{n,\text{free}} L}{\sqrt{f_{n,\text{free}}}} \quad (2.70)$$

In case of small contact damping, its influence on the contact-resonance frequency can be neglected, and the contact function reduces to $\phi(\alpha) \approx 3k^*/k_C$. One obtains an analytical formula to calculate the normalized contact stiffness k^*/k_C directly from the contact-resonance frequencies [105].

$$\frac{k^*}{k_C} = 3 \frac{(c_n \sqrt{f_n})^3 c h^+ (c_n \sqrt{f_n})}{c h^- (c_n \sqrt{f_n} L_1/L) \text{mix}^- (c_n \sqrt{f_n} L_2/L) - c h^+ (c_n \sqrt{f_n} L_2/L) \text{mix}^- (c_n \sqrt{f_n} L_1/L)} \quad (2.71)$$

However, the position of the sensor-tip is usually not known. If one measures the contact-resonance frequencies of two flexural modes and assumes that the contact stiffness is the same for both modes, one can calculate the sensor-tip position numerically [105].

If lateral forces are considered, the quadratic equation must be solved:

$$\begin{aligned} \phi(\alpha) &= g \pm \sqrt{g^2 - \frac{L_1^2 L_1^4 S_4}{h^2 S_0 c_P}} \\ &\quad L_1 S_1 (\cos^2 \varphi + c_P \sin^2 \varphi) + L_1^2 S_2 \frac{h}{L_1} (c_P - 1) \sin \varphi \cos \varphi \\ &\quad + L_1^3 S_3 \frac{h^2}{L_1^2} (\sin^2 \varphi + c_P \cos^2 \varphi) \\ g &= - \frac{\quad}{2 S_0 \frac{h^2}{L_1^2} c_P} \end{aligned} \quad (2.72)$$

Here g is only an auxiliary quantity. In principle the normalized contact stiffness k^*/k_C can again be calculated if the contact damping is low. However, the tilt angle φ of the cantilever, the height h of the sensor tip with relation to the cantilever length L , and the ratio $c_P = \phi_{\text{Lat}}/\phi \approx k_{\text{Lat}}^*/k^*$ of lateral to normal contact constants must be known. The tilt angle φ is technically defined by the cantilever holder in the AFM. The height of the sensor tip is usually specified by the manufacturer of the commercial probes. The length of the cantilever beam can be measured with an optical microscope. A more precise measurement of the tip height is only possible with a scanning electron microscope. Instead of calculating the contact stiffness from the contact-resonance frequencies, one can also use the formulas for the forced vibration and fit the experimental resonances to the theoretical curves by parameter variation [60, 90]. Because of the various unknown parameters, however, the error in the obtained contact stiffness values can be high.

In contrast to the other parameters, the ratio between the lateral and the normal stiffness c_P is not a parameter of the instrument, but depends on the elastic constants of the sensor tip, on the local elastic constants of the sample, and the other tip-sample interaction forces. If c_P is unknown, care should be taken to work in the range of the dispersion curves where the influence of the lateral forces is low (see Chap. 4.1). The lateral forces shift the resonant frequencies of the modes in a different way than the normal forces. Therefore it should be possible to determine normal and lateral contact stiffness by fitting the measured spectra to the simulated spectra. However, up to now, as discussed in Chap. 2.3, real cantilever beams do not agree perfectly with the analytical model. On the other hand, the lateral contact stiffness can in

principle be measured if torsional or lateral contact-resonance experiments are made at the same location of the sample.

2.8.1

Experiments for Quantitative Evaluation

For quantitative evaluation the resonant frequencies of the clamped-free beam are needed. As far as the bandwidth is sufficient the free resonant frequencies can be measured with the internal sweep programs of the commercial instruments. Alternatively an optical interferometer as described in Chap. 2.3 can be used. Two flexural modes are necessary at minimum. However, it is better to determine the resonant frequencies of more flexural modes in order to test how much the cantilever deviates from the model of the clamped-free beam. Then the sensor tip is brought into contact with a sample and a predefined static deflection is set by the operator. The contact-resonance frequencies of at least two modes are measured by sweeping the frequency with the help of the AFAM or UAFM set-up described in Chap. 2. The amplitude of excitation should be kept as small as possible in order to avoid nonlinearities in the spectrum. As contact-resonance frequencies use to shift as a function of applied load, variation of the applied static load helps to distinguish contact resonances from other signals. An example of contact-resonance spectra of three flexural modes and with three different static deflections of the cantilever is shown in Fig. 2.24.

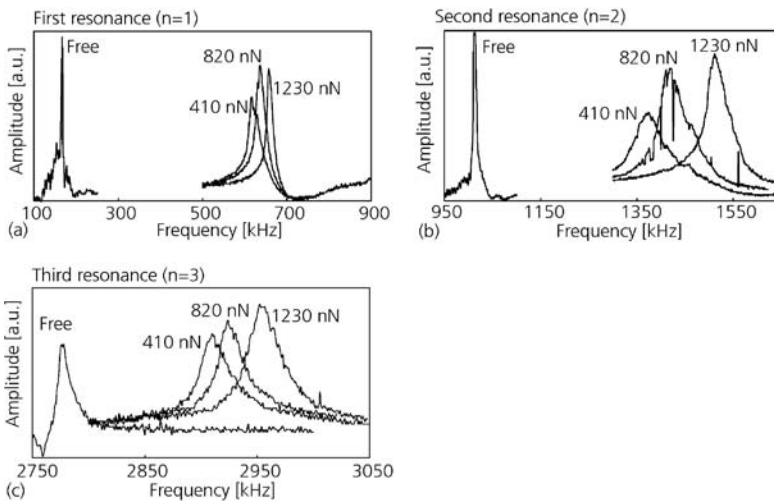


Fig. 2.24. Contact-resonance spectra measured with a silicon cantilever of 41 N/m spring constant on a silicon single crystal [103]. The resonances of the clamped-free beam and contact resonances of the first three flexural modes are shown. The static load for the contact resonances was 410 nN, 820 nN, and 1230 nN. It can be seen that all contact-resonance frequencies are higher than the corresponding free resonance and that the contact-resonance frequencies increase with increasing static load

The sensor-tip position L_1 on the length axis of the cantilever is then calculated numerically. It is assumed that the normalized contact stiffness which is calculated using (2.71) or (2.72) from the measured contact-resonance frequencies must be the same for all contact modes if the static load is identical. If more than two modes are measured, the obtained tip position will in most cases be different for each pair of modes. These differences yield the systematic error in the normalized contact stiffness k^*/k_C which typically amounts to 20% up to 40% at present. The systematic error is caused by the deviation of the real cantilever from the analytical model. After having determined the normalized contact stiffness one has to apply a model for the tip-sample force interaction to obtain an elastic constant of the surface.

An elastic constant of the sample surface can be calculated from k^*/k_C using the contact mechanical formulas (2.19) and (2.20) or (2.23), if the spring constant of the cantilever, the normal load, and the elastic constants of the sensor tip and its radius are known. Usually these constants are not known precisely enough, and reference measurements on samples with known elastic constants are necessary. Figure 2.25 shows a sequence of measurements on two silicon single crystal surfaces with different orientation [82]. A reproducible difference between the contact-resonance frequencies of the two surfaces is visible, but also an average increase in the contact-resonance frequencies and in the contact stiffness. The increase in contact stiffness is caused by tip wear [62, 79, 106]. Often the contact-resonance frequency increases strongly during the first measurements. A more stable situation is reached after the tip has been rounded so much that the pressure in the contact area is reduced sufficiently to stop further tip damage. The different symbols in Fig. 2.25 belong to different static cantilever loads. As can be seen, the static force has a strong influence

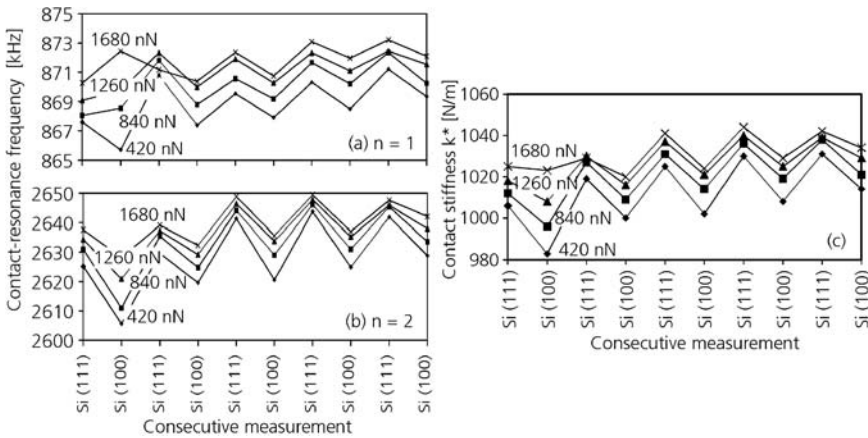


Fig. 2.25. Sequence of contact-resonance measurements on two different silicon single crystal surfaces of different orientation [82]. The contact-resonance frequencies of the first two flexural modes are shown (a) and (b). Four different static loads of the cantilever, 420 nN, 840 nN, 1260 nN, and 1680 nN were chosen. The contact stiffness k^* calculated from (a) and (b) is shown (c). The cantilever made of silicon single crystal with the dimensions $120 \times 30 \times 2.8 \mu\text{m}^3$ (length \times width \times thickness) had a spring constant of 42 N/m. The first two clamped-free resonant frequencies of the sensor were 287.96 kHz and 1596.37 kHz

on the contact-resonance frequency. The shift of the contact stiffness as a function of applied load can be used to estimate the shape of the sensor tip [56]. If the sensor tip is broken, so that the end of the tip is flat, the contact-resonance frequencies do not shift any more as a function of applied load. A flat tip could be an advantage, because in this case the contact area would be constant and known. On the other hand it is difficult to align a flat tip parallel to the sample surface.

By comparison of the normalized contact stiffness on the two samples, the difference of the elastic constants can be calculated. When the normal load F_n and the tip radius R are identical for a measurement on a sample of interest and on a reference sample, one can conclude from the Hertzian model, (2.19):

$$E^* = E_{\text{Ref}}^* \cdot \sqrt{\frac{k^*}{k_{\text{Ref}}^*}^3} \quad (2.73)$$

Here E_{Ref}^* and k_{Ref}^* are the reduced Young's modulus and the contact stiffness of the reference sample, respectively. A simpler expression, $E^* = E_{\text{Ref}}^* \cdot k^*/k_{\text{Ref}}^*$, holds in the case of a flat tip. The indentation modulus of the sample M_S can be calculated by solving (2.23): $M_S^{-1} = E^{*-1} - M_T^{-1}$. In case of an isotropic sample with known Poisson's ratio the Young's modulus follows directly from M_S using (2.20). The indentation modulus of the tip can be calculated from the elastic single crystal constants of the tip material if they are known, or it can be measured using two reference samples:

$$M_T = \frac{M_1 M_2 \left(1 - \sqrt{k_1^{*3}/k_2^{*3}}\right)}{M_2 \sqrt{k_1^{*3} k_2^{*3}} - M_1} \quad (2.74)$$

Here M_1 , M_2 , k_1^* , and k_2^* are the indentation modulus and the contact stiffness of reference samples 1 and 2, respectively. The steps for quantitative measurements are summarized schematically in Fig. 2.26.

By comparison of the contact stiffness on two samples the difference in the elastic constants can be determined. The elastic contact generates shear stresses and compressional stresses in the tip and the sample. The anisotropy in the indentation

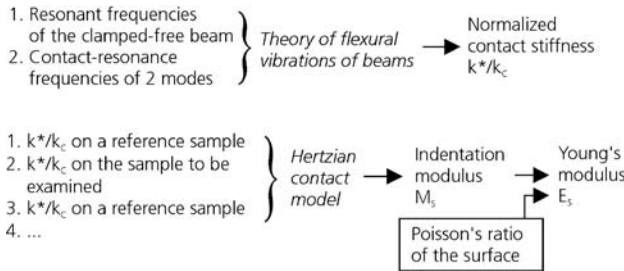


Fig. 2.26. Schematic list showing the measurements and steps of evaluation which are necessary to obtain quantitative elastic constants of a sample surface

modulus is therefore lower than the anisotropy in the Young's modulus. It was shown for silicon single crystal surfaces with two different orientations that the measured difference in contact stiffness k^* agreed with the difference in k^* predicted by the indentation modulus calculated from the elastic single crystal constants of silicon [82]. Nanocrystalline ferrites [105], diamond like carbon thin films [79], and clay minerals [107] were examined by contact-resonance spectroscopy. Figure 2.27 shows contact-resonance spectra on polystyrene, clay, mica and fused silica [107]. Polystyrene and fused silica were chosen as reference materials. Clay minerals fill the pores between fused silica grains in sandstone. They influence the average elastic constants of sand stone strongly, but measurement of their elastic constants is not easy. With the AFAM-measurements it was possible to estimate the Young's modulus of the clay minerals. Dupas et al. imaged WC and Co-Phases in WC-Co Cermets and examined NiTi-epoxy composites by contact-resonance spectroscopy. They obtained quantitative results by fitting the measured spectra to simulations [60]. Hurley et al. examined the elastic constant of a niobium film quantitatively by AFAM [64], and Hurley and Turner investigated the influence of ambient humidity on quantitative AFAM results [108].

Piezoelectric ceramics like BaTiO₃ and PZT were investigated by AFAM and the domain contrast was examined [83]. The indentation modulus of BaTiO₃ ceramics and PZT ceramics was calculated and compared to experiments [83]. Tsuji et al. evaluated the stiffness of domain boundaries in piezoelectric material by UAFM [109].

Up to the present, commercially available cantilevers have large tolerances in their dimensions and they do not behave perfectly like a clamped beam. Therefore reliable quantitative measurements are only possible if one chooses reference samples with elastic constants close to the constants of the sample of interest. In addition, the error in the obtained values for the elastic constants depends on the control of the static load. It is essential for the calibration by reference sample to compare measurements that are made with the same normal load. In most commercial instruments, however, there is no possibility to apply a calibrated force to the cantilever.

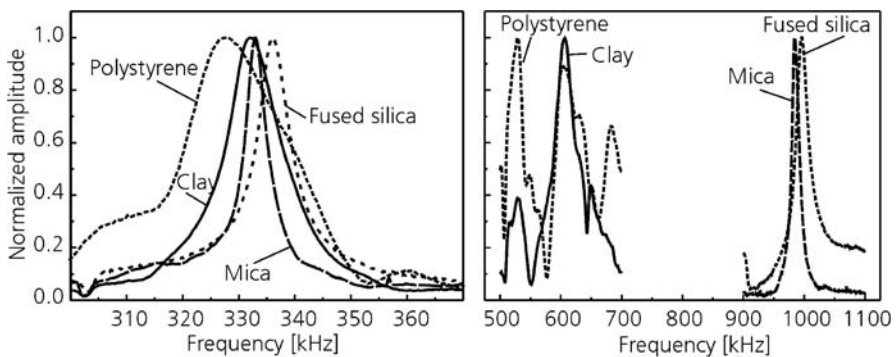
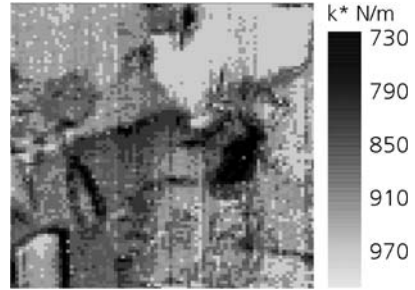


Fig. 2.27. Contact-resonance spectra on polystyrene, clay, mica and fused silica [104]. The spectra of the first and the second contact-resonance frequency of a cantilever with a spring constant of 1.5 N/m are shown

Fig. 2.28. Contact stiffness image of a nanocrystalline nickel sample. The contact stiffness values were calculated from contact-resonance frequencies. The size of the image is $1.5 \times 1.4 \mu\text{m}^2$. The spring constant of the employed cantilever was 48 N/m and its free resonant frequencies were 166 kHz and 1031 kHz for the first and the second flexural mode, respectively



The force is applied indirectly by approaching the sample and the fixed end of the cantilever. Due to the tilt of the cantilever with respect to the surface, the cantilever buckles and the static bending depends on the normalized contact stiffness k^*/k_C . Because of the different amount of buckling identical static beam-deflection signals do not correspond to identical normal loads F_n if the elastic constants of the samples differ strongly.

With the new imaging techniques discussed in Chap. 6 it is possible to obtain contact-resonance images instead of only amplitude images. From two resonant frequency images of two different modes one can calculate a contact stiffness image as shown in Fig. 2.28 and an indentation modulus image if reference measurements are available [101, 102].

2.9

Nonlinear Forces

A simple force curve contains an attractive adhesive part and a repulsive elastic part [110, 111]. In AFM in air, adhesion forces caused by a water meniscus dominate and drop almost to zero when the water meniscus breaks. When the amplitude of vibration is slowly increased, the nonlinearity of the force is more and more sensed by the AFM. The resonance curves develop a steep edge at the left side of the spectrum, the maximum shifts to lower frequencies and an amplitude jump is noticed with hysteresis when the direction of the frequency scan is inverted [62]. An example of contact-resonance spectra measured with different amplitudes of excitation is shown in Fig. 2.29.

It has been shown that the contribution of the local elasticity and the adhesion to the contact forces can be separated by exploiting the amplitude dependence of the resonant frequency, the so-called backbone curve [112]. In the regime of small nonlinearity, when the tip remains in contact with the sample surface during its vibration cycle, the cantilever vibration behavior resembles that of a macroscopic Hertzian contact oscillator [113]. The harmonic balance method [112] or the multiple scales technique [74] can be applied to solve the equation of motion approximately. Amplitude jumps caused by bistability are typical for a nonlinear system with softening behavior [114].

If the amplitude of surface vibration is increased, one can observe that the high frequency amplitude of the cantilever first increases linearly. After a certain thresh-

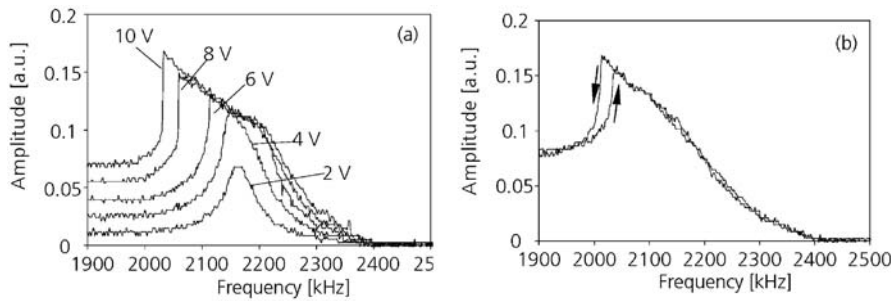


Fig. 2.29. Contact-resonance spectra showing the influence of the nonlinear forces [62]. (a) When the excitation amplitude of the transducer is increased, the spectra become asymmetric and develop a steep edge. (b) Hysteresis depending on the direction of the frequency scan

old, however, the minimum of the force curve is passed through during a vibration cycle and the amplitude of vibration of the cantilever remains constant or even decreases [115]. At the same time a DC offset of the cantilever develops, i.e. the sensor tip lifts off the sample surface. In this amplitude region UFM and SAFM are operating. At very high amplitudes the tip jumps so far away from the sample surface that the water meniscus breaks and the interaction forces drop almost to zero during a vibration cycle. The contact with the sample can now be considered as an impact where the impact time is short compared to the period of oscillation. In this regime subharmonics have been observed [116] and the ultrasonic mode resembles the intermittent contact or tapping mode where the vibration is excited by the transducer in the cantilever holder. Different authors have examined the influence of the nonlinear forces on the spectrum of the first flexural resonance in the tapping mode and in the non-contact mode [117–119]. Recently Stark et al. applied a state-space model to examine flexural vibration spectra in the tapping mode including the higher modes [120].

2.10 Conclusions

Analytical models to describe flexural cantilever vibration for quantitative measurement of elastic constants have been summarized in this article. Examples of application by different research groups have been given.

The challenge in quantitative AFAM will be to manufacture and model sensors in such a way that a characterization of every individual sensor by electron microscopy is not necessary. Furthermore, sensor tips with a well defined radius, a high stiffness and a high resistance to breaking and wear must be developed. Imaging techniques which acquire the contact-resonance frequency or full spectra in every point of the surface are more favorable than mere amplitude or phase imaging. Such techniques will make it possible to map local surface stiffness and contact damping quantitatively. In cases where high local resolution is not required, the precision of nanoindentation with regard to quantitative Young's modulus will probably be higher, because nanoindentation provides calibrated force measurements and forces

normal to the surface. On the other hand, the development of contact mechanics models for dynamic indentation is an active area of research, where nanoindentation and the AFM-techniques can stimulate each other. The potential of the high frequency AFM techniques like AFAM and UAFM is local resolution in the nm-range which can in principle be achieved, the possibility of fast image acquisition and the possibility to examine frequency-dependent phenomena. Furthermore, the measurement of frequencies is an advantage, as it avoids difficult calibration of amplitude. By combination of the results from different bending, lateral bending and torsional modes, elastic constants in three directions relative to the sample surface can be measured by AFM.

Nonlinear tip-sample forces such as friction and adhesion change the shape of the resonance curves in a characteristic way. Quantitative evaluation of nonlinear resonance curves is a still larger challenge than elasticity measurement. Numerical modeling and absolute measurement of the vibration amplitudes of tip and sample will be required in this case.

Acknowledgements. The author would like to thank W. Arnold, all colleagues, coworkers, and students for support and collaboration. Critical proofreading of this manuscript by S. Hirsekorn is gratefully acknowledged. Part of this work was supported by the German ministry of education and research (BMBF) in the frame of the research program “Nanoanalytik” under the contract No. FKZ13N8326.

A Appendix

A.1 Definitions

In order to calculate the forced vibration for the model shown in Fig. 2.8, including the angle φ of the cantilever, lateral forces, and tip position, abbreviations are defined for combinations of the trigonometric and hyperbolic functions which are needed frequently:

$$\begin{aligned}
 s_1^\pm &= \sin \alpha L_1 \pm \sinh \alpha L_1 & s_2^\pm &= \sin \alpha L_2 \pm \sinh \alpha L_2 \\
 c_1^\pm &= \cos \alpha L_1 \pm \cosh \alpha L_1 & c_2^\pm &= \cos \alpha L_2 \pm \cosh \alpha L_2 \\
 ssh_1 &= \sin \alpha L_1 \sinh \alpha L_1 & ssh_2 &= \sin \alpha L_2 \sinh \alpha L_2 \\
 cch_1 &= \cos \alpha L_1 \cosh \alpha L_1 & cch_2 &= \cos \alpha L_2 \cosh \alpha L_2 \\
 cch_1^\pm &= 1 \pm \cos \alpha L_1 \cosh \alpha L_1 & cch_2^\pm &= 1 \pm \cos \alpha L' \cosh \alpha L' \\
 cch_{1+2}^+ &= 1 + \cos \alpha (L_1 + L_2) \cosh \alpha (L_1 + L_2) \\
 mix_1^\pm &= \sin \alpha L_1 \cosh \alpha L_1 \pm \cos \alpha L_1 \sinh \alpha L_1 \\
 mix_2^\pm &= \sin \alpha L_2 \cosh \alpha L_2 \pm \cos \alpha L_2 \sinh \alpha L_2
 \end{aligned} \tag{A.1}$$

As can be seen in Table 2.3, the formulas for the forced vibration excited by a concentrated force acting at the free end of the beam are very similar to the solutions in

Table 2.3 case (b), excitation by surface vibration. Therefore only the UAFM-mode and AFAM-mode are calculated here. In both cases, the calculation is based on the equation of motion (2.1), the dispersion relation (2.5) and the solution (2.3). The definitions of the contact functions $\phi(\alpha)$ and $\phi_{\text{Lat}}(\alpha)$, the dimensionless contact damping p and the auxiliary functions X , T , and U in (2.33)–(2.38) are not repeated here. They can be taken from the main body of the text. As discussed in Chap. 4, two functions $y(x)$ and $y_2(x_2)$ are defined for the two sections of the beam from the clamped end to the tip position and from the free end to the tip position, respectively.

A.2

UAFM-mode

In case of a vertical vibration of the clamped end of the beam the boundary conditions are:

$$\begin{aligned}
 x = 0 : & \begin{cases} (x) = u_0 \\ \frac{\partial y(x)}{\partial x} = 0 \end{cases} & x_2 = 0 : & \begin{cases} \frac{\partial^2 y_2(x_2)}{\partial x_2^2} = 0 \\ \frac{\partial^3 y_2(x_2)}{\partial x_2^3} = 0 \end{cases} \\
 x = L_1 \text{ or } x_2 = L_2 : & \begin{cases} y(x) = y_2(x_2) \\ \frac{\partial y(x)}{\partial x} = -\frac{\partial y_2(x_2)}{\partial x_2} \end{cases} \\
 x = L_1 \text{ or } x_2 = L_2 : & \begin{cases} \frac{\partial^2 y(x)}{\partial x^2} - \frac{\partial^2 y_2(x_2)}{\partial x_2^2} = -T(\alpha) \frac{\partial y(x)}{\partial x} - X(\alpha) y(x) \\ \frac{\partial^3 y(x)}{\partial x^3} + \frac{\partial^3 y_2(x_2)}{\partial x_2^3} = U(\alpha) \cdot y(x) + X(\alpha) \frac{\partial y(x)}{\partial x} \end{cases}
 \end{aligned} \tag{A.2}$$

By combining the functions $y(x)$ and $y_2(x_2)$ and the first four boundary conditions one obtains:

$$\begin{aligned}
 y(x) &= \frac{u_0}{2} (\cos \alpha x + \cosh \alpha x) + A_2 (\cos \alpha x - \cosh \alpha x) + A_4 (\sin \alpha x - \sinh \alpha x) \\
 y_2(x_2) &= A_1 (\cos \alpha x_2 + \cosh \alpha x_2) + A_3 (\sin \alpha x_2 + \sinh \alpha x_2)
 \end{aligned} \tag{A.3}$$

The remaining four boundary conditions together with these solutions lead to a linear system of equations with four unknown constants A_1 , A_2 , A_3 and A_4 . Solving the linear system for the constants leads to:

$$\begin{aligned}
 A_1 &= \frac{u_0}{N(\alpha)} \{ -2\alpha^5 c_{1+2}^- - \alpha^4 T c_2^+ s_1^+ + \alpha^3 X (s_2^+ s_1^+ + c_2^+ c_1^-) - \alpha^2 U s_2^+ c_1^- \} \\
 A_2 &= \frac{u_0}{N(\alpha)} \{ 2\alpha^5 ssh_{1+2} + \alpha^4 T (ssh_1 mix_2^+ + mix_1^- cch_2^+) \\
 &\quad - 2\alpha^3 X (ssh_1 ssh_2 + cch_1 cch_2^+) + \alpha^2 U (ssh_1 mix_2^- - mix_1^+ cch_2^+) \\
 &\quad - \alpha(TU - X^2) ssh_1 cch_2^+ \}
 \end{aligned}$$

$$\begin{aligned}
A_3 &= \frac{u_0}{N(\alpha)} \left\{ -2\alpha^5 c_{1+2}^- - \alpha^4 T s_2^- s_1^+ + \alpha^3 X (-c_2^+ s_1^+ + s_2^- c_1^-) + \alpha^2 U c_2^+ c_1^- \right\} \\
A_4 &= \frac{u_0}{N(\alpha)} \left\{ -2\alpha^5 \text{mix}_{1+2}^+ - \alpha^4 T (2\text{ssh}_1 cch_2^+ + \text{mix}_1^+ \text{mix}_2^+) \right. \\
&\quad \left. - 2\alpha^3 X (\text{mix}_1^- cch_2^+ - \text{mix}_1^+ \text{ssh}_2) \right\}
\end{aligned} \tag{A.4}$$

With the common denominator $N(\alpha)$:

$$\begin{aligned}
N(\alpha) &= 2\{-2\alpha^5 cch_{1+2}^+ + \alpha^4 T(\text{mix}_2^+ cch_1^- - cch_2^+ \text{mix}_1^+) \\
&\quad - 2\alpha^3 X(cch_2^+ \text{ssh}_1 + \text{ssh}_2 cch_1^-) + \alpha^2 U(\text{mix}_2^- cch_1^- - cch_2^+ \text{mix}_1^-) \\
&\quad - \alpha(TU - X^2)cch_2^+ cch_1^-\}
\end{aligned} \tag{A.5}$$

If the sensor tip is located at the end of the beam ($L_2 = 0$), the constants and the denominator simplify to:

$$\begin{aligned}
A_2 &= \frac{u_0}{2N_0(\alpha)} \left\{ -\alpha^4 \text{ssh} - \alpha^3 T \text{mix}^- + 2\alpha^2 X cch + \alpha U \text{mix}^+ + (TU - X^2) \text{ssh} \right\} \\
A_4 &= \frac{u_0}{2N_0(\alpha)} \{ \alpha^4 \text{mix}^+ + 2\alpha^3 T \text{ssh} + 2\alpha^2 X \text{mix}^- - 2\alpha U cch \\
&\quad - (TU - X^2) \text{mix}^+ \} N_0(\alpha) = \alpha^4 cch^+ + \alpha^3 T \text{mix}^+ + 2\alpha^2 X \text{ssh} \\
&\quad + \alpha U \text{mix}^- + (TU - X^2) cch^-
\end{aligned} \tag{A.6}$$

The amplitude and the slope at the end of the beam ($x = L$) are in this case ($L_2 = 0$):

$$\begin{aligned}
y(L, \alpha) &= \frac{u_0}{N_0(\alpha)} \{ \alpha^4 c^+ + \alpha^3 T s^+ - \alpha^2 X c^- \} \\
\frac{\partial y}{\partial x}(L, \alpha) &= \alpha \frac{u_0}{N_0(\alpha)} \{ \alpha^4 s^- - \alpha^2 X s^+ + \alpha U c^- \}
\end{aligned} \tag{A.7}$$

The forced vibration in the UAFM-mode with lateral forces and tilt of the cantilever, but without variable tip position, was discussed in a publication [121]. Unfortunately, there are several typewriting errors in the formulas in this publication. The correct boundary conditions were published for example in [104].

A.3 AFAM-mode

In the case of vibration of the surface in its normal direction, one obtains components of excitation in vertical direction (y -direction) and in lateral direction (x -direction) in the coordinate system of the cantilever. The formulas derived here can also be used for excitation of flexural modes by lateral surface vibration. The components of excitation in the coordinate system of the cantilever need only to be changed in this case. In case of normal surface vibration the boundary conditions are:

$$\begin{aligned}
x = 0 : & \begin{cases} y(x) = 0 \\ \frac{\partial y(x)}{\partial x} = 0 \end{cases} & y = L : & \begin{cases} \frac{\partial^2 y}{\partial x^2} = 0 \\ \frac{\partial^3 y}{\partial x^3} = 0 \end{cases} \\
x = L_1 \text{ or } x_2 = L_2 : & \begin{cases} y(x) = y_2(x_2) \\ \frac{\partial y(x)}{\partial x} = -\frac{\partial y_2(x_2)}{\partial x_2} \end{cases} \\
x = L_1 \text{ or } x_2 = L_2 : & \begin{cases} \frac{\partial^2 y(x)}{\partial x^2} - \frac{\partial^2 y_2(x_2)}{\partial x_2^2} = a_0 - T(\alpha) \frac{\partial y(x)}{\partial x} - X(\alpha) y(x) \\ \frac{\partial^3 y(x)}{\partial x^3} + \frac{\partial^3 y_2(x_2)}{\partial x_2^3} = -b_0 + U(\alpha) \cdot y(x) + X(\alpha) \frac{\partial y(x)}{\partial x} \end{cases}
\end{aligned} \tag{A.8}$$

With the components of excitation in the coordinate system of the cantilever:

$$a_0 = -u_0 \frac{h}{L_1^3} \phi_{\text{Lat}}(\alpha) \sin \varphi \quad b_0 = u_0 \frac{1}{L_1^3} \phi(\alpha) \cos \varphi \tag{A.9}$$

Using the first four boundary conditions one obtains the following solutions for the two sections of the cantilever:

$$\begin{aligned}
y(x) &= A_2(\cos \alpha x - \cosh \alpha x) + A_4(\sin \alpha x - \sinh \alpha x) \\
y_2(x_2) &= A_1(\cos \alpha x_2 + \cosh \alpha x_2) + A_3(\sin \alpha x_2 + \sinh \alpha x_2)
\end{aligned} \tag{A.10}$$

The constants are again calculated using the four boundary conditions at the tip position and solving the linear system of equations for the constants A_1 , A_2 , A_3 , and A_4 :

$$\begin{aligned}
A_1 &= \left\{ -\alpha^3 a_0 [c_2^+ ssh_1 + s_2^+ mix_1^+ + c_2^- cch_1^-] - \alpha^2 b_0 [c_2^+ mix_1^- + s_2^+ ssh_1 - s_2^- cch_1^-] + \alpha (Xa_0 - Tb_0) c_2^+ cch_1^- + (Xb_0 - Ua_0) s_2^+ cch_1^- \right\} / N(\alpha) \\
A_2 &= \left\{ -\alpha^3 a_0 [mix_2^+ s_1^- + ssh_2 c_1^- - cch_2^+ c_1^+] + \alpha^2 b_0 [mix_2^- c_1^- + ssh_2 s_1^- + cch_2^+ s_1^+] + \alpha (Xa_0 - Tb_0) cch_2^+ c_1^- - (Xb_0 - Ua_0) cch_2^+ s_1^- \right\} / N(\alpha) \\
A_3 &= \left\{ \alpha^3 a_0 [c_2^+ mix_1^+ - s_2^- ssh_1 - s_2^- cch_1^-] - \alpha^2 b_0 [-c_2^+ ssh_1 + s_2^- mix_1^- + c_2^- cch_1^-] + \alpha (Xa_0 - Tb_0) s_2^- cch_1^- - (Xb_0 - Ua_0) c_2^+ cch_1^- \right\} / N(\alpha) \\
A_4 &= \left\{ \alpha^3 a_0 [-ssh_2 s_1^+ + mix_2^+ c_1^- - cch_2^+ s_1^-] + \alpha^2 b_0 [-ssh_2 c_1^- + mix_2^- s_1^+ - cch_2^+ c_1^+] + \alpha (Xa_0 - Tb_0) cch_2^+ s_1^+ + (Xb_0 - Ua_0) cch_2^+ c_1^- \right\} / N(\alpha)
\end{aligned} \tag{A.11}$$

The denominator $N(\alpha)$ is the same as in the UAFM-mode (A.5). If the position detector is located at the end of the beam ($x_2 = 0$), the solution simplifies to:

$$y_2(0) = 2A_1 \frac{\partial y_2}{\partial x_2}(0) = -2\alpha A_3 \tag{A.12}$$

References

1. Hurley DC, Tewary VK, and Richards AJ (2001) *Meas Sci Technol* 12:1486
2. Every AG (2002) *Meas Sci Technol* 13:R21
3. Zieniuik JK and Latuszek A (1989) in: Shimizu H, Chubachi N, Kushibiki J (eds) *Acoust Img* 17. Plenum Press, New York, p 219
4. Khuri-Yakub BT, Cinbis C, Chou CH, Reinholdtsen PA (1989) in: McAvoy BR (ed) *Proc. IEEE Ultrasonics Symp*, p 805
5. Kulik A, Attal J, Gremaud G (1993) in: Wei Y and Gu B (eds) *Acoustical Imaging* 20. Plenum Press, New York, p 241
6. Quate CF, Khuri-Yakub BT, Akamine S, Hadimioglu BB (1994) *United States Patent* 5,319,977
7. Günther P, Fischer UCh, Dransfeld K (1998) *Appl Phys B* 48:89
8. Giessibl FJ (1998) *Appl Phys Lett* 73:3956
9. Binnig G, Quate CF, Gerber Ch (1986) *Phys Rev Lett* 56:930
10. Kolosov O and Yamanaka K (1993) *Jpn J Appl Phys* 32:22
11. Chilla E, Hesjedahl T, Fröhlich H-J (1997) *Phys Rev B* 55:15852
12. Rabe U and Arnold W (1994) *Appl Phys Lett* 64:1493
13. Yamanaka K and Nakano S (1996) *Jpn J Appl Phys* 35:3787
14. Rohrbeck W and Chilla E (1992) *Phys stat sol (a)* 131:69
15. Hesjedahl T and Behme G (2001) *Europhys Lett* 54:154
16. Yamanaka K, Ogiso H, Kolosov O (1994) *Jpn J Appl Phys* 33:3197
17. Kolosov OV, Castell MR, Marsh CD, Briggs GAD, Kamins TI, Williams RS (1998) *Phys Rev Lett* 81:1046
18. Yamanaka K (1996) *Thin Solid Films* 273:116
19. Inagaki K, Kolosov OV, Briggs GAD, Wright OB (2000) *Appl Phys Lett* 76:1836
20. Inagaki K, Matsuda O, Wright OB (2002) *Appl Phys Lett* 80:2386
21. Huey BD (2002) in: Maev RG (ed) *Acoust Img* 26. Kluwer Academic/Plenum Publishers, p 183
22. Dinelli F, Castell MR, Ritchie DA, Mason NJ, Briggs GAD, Kolosov OV (2000) *Phil Mag A* 80:2299
23. Maivald P, Butt H-J, Gould SAC, Prater CB, Drake B, Gurley JA, Elings VB, Hansma PK (1991) *Nanotechnology* 2:103
24. Florin E-L, Radmacher M, Fleck B, Gaub HE (1994) *Rev Sci Instr* 65:639
25. Mazeran P-E and Loubet J-L (1997) *Tribol Lett* 3:125
26. Arinero R and Lévêque G (2003) *Rev Sci Instr* 74:104
27. Troyon M, Wang Z, Pastre D, Lei HN, Hazotte A (1997) *Nanotechnology* 8:163
28. Rosa A, Weilandt E, Hild S, Marti O (1997) *Meas Sci Technol* 8:1
29. Burnham NA, Kulik AJ, Gremaud G, Gallo PJ, Oulevey F (1996) *J Vac Sci Technol B* 14:794
30. Oulevey F, Gremaud G, Mari D, Kulik AJ, Burnham NA, Benoit W (2000) *Scripta mater* 42:31
31. Elings VB and Gurley JA (1993) *US Patent No.* 5,266,801
32. Hirsekorn S, Rabe U, Arnold W (2001) *Appl Phys A* 72 [Suppl.]:S87
33. Cretin B and Sthal F (1993) *Appl Phys Lett* 62:829
34. Robert L and Cretin B (1999) *Surf Interface Anal* 27:568
35. Vairac P and Cretin B (1996) *Appl Phys Lett* 68:461
36. Cretin B and Vairac P (1997) *Appl Phys Lett* 71:2082
37. Oliver WC and Pharr GM (1992) *J Mater Res* 7:1564
38. Lorenz D, Fränzel W, Einax M, Grau P, Berg G (2001) *J Mater Res* 16:1776
39. Seyed Asif SA, Wahl KJ, Colton RJ, Warren OL (2001) *J Appl Phys* 90:1192
40. Bushan B and Li X (2003) *Int Mater Rev* 48:125

41. Butt H-J and Jaschke M (1995) *Nanotechnology* 6:1
42. Salapaka MV, Bergh HS, Lai J, Majumdar A, McFarland E (1997) *J Appl Phys* 81:2480
43. Rabe U, Janser K, Arnold W (1996) in: Tortoli P and Masotti L (eds) *Acoustical Imaging* 22. Plenum Press, New York, p 669
44. Rabe U, Janser K, Arnold W (1996) *Rev Sci Instr* 67:3281
45. Meyer G and Amer NM (1990) *Appl Phys Lett* 57:2089
46. Marti O, Colchero J, Mlynek J (1990) *Nanotechnology* 1:141
47. Kawagishi T, Kato A, Hoshi Y, Kawakatsu H (2002) *Ultramicroscopy* 91:37
48. Pfeiffer O, Bennewitz R, Baratoff A, Meyer E (2002) *Phys Rev B* 65:161403
49. Reinstädter M, Rabe U, Scherer V, Hartmann U, Goldade A, Bushan B, Arnold W (2003) *Appl Phys Lett* 82:2604
50. Krottil HU, Weilandt E, Stifter Th, Marti O, Hild S (1999) *Surf Interface Anal* 27:341
51. Caron A, Rabe U, Reinstädter M, Turner JA, Arnold W (2004) *Appl Phys Lett* 85:6398
52. Drobeck T, Stark RW, Gräber M, Heckl WM (1999) *New J Phys* 1:15.1
53. Drobeck T, Stark RW, Heckl W (2001) *Phys Rev B* 64:045401
54. Yamanaka K and Nakano S (1998) *Appl Phys A* 66:S313
55. Yamanaka K, Noguchi A, Tsuji T, Koike T, Goto T (1999) *Surf Interface Anal* 27:600
56. Yamanaka K, Tsuji T, Noguchi A, Koike T, Mihara T (2000) *Rev Sci Instr* 71:2403
57. Crozier KB, Yarialioglu GG, Degertekin FL, Adams JD, Minne SC, Quate CF (2000) *Appl Phys Lett* 76:1950
58. Yarialioglu GG, Degertekin FL, Crozier KB, Quate CF (2000) *J Appl Phys* 87:7491
59. Crozier KB, Yarialioglu GG, Degertekin FL, Adams JD, Minne SC, Quate CF (2000) *Proc SPIE* 4099:48
60. Dupas E, Gremaud G, Kulik A, Loubet J-L (2001) *Rev Sci Instr* 72:3891
61. Rabe U and Arnold W (1994) *Ann Phys* 3:589
62. Rabe U, Kester E, Arnold W (1999) *Surf Interface Anal* 27:386
63. Stark RW, Drobeck T, Heckl WM (2001) *Ultramicroscopy* 86:207
64. Hurley DC, Shen K, Jennett NM, Turner JA (2003) *J Appl Phys* 94:2347
65. Turner JA and Wiehn JS (2001) *Nanotechnology* 12:322
66. Weaver W, Timoshenko SP, Young DH (1990) *Vibration Problems in Engineering*. John Wiley, New York
67. Stokey FW (1976) *Vibration of Systems Having Distributed Mass and Elasticity*. In: Harris CM, Crede CE (eds) *Shock and Vibration Handbook*. McGraw-Hill, New York, Chapter 7
68. Radmacher M, Tillmann RW, Gaub HE (1993) *Biophys J* 64:735
69. Burnham NA, Gremaud G, Kulik AJ, Gallo P-J, Oulevey F (1996) *J Vac Sci Technol B* 14:1308
70. Turner JA, Hirsekorn S, Rabe U, Arnold W (1997) *J Appl Phys* 82:966
71. Reinstädter M, Rabe U, Scherer V, Turner JA, Arnold W (2003) *Surf Sci* 532-535:1152
72. Hoummady M, Farnault E, Yahiro T, Kawakatsu H (1997) *J Vac Sci Technol B* 15:1539
73. Monchalin J-P (1986) *IEEE Transactions UFFC* 33:485
74. Turner JA and Hurley DC (2003) *Instrumentation, Mesure, Métrologie* 3:117
75. Reinstädter M (2004) *Elastische und tribologische Oberflächencharakterisierung auf der Nanoskala mittels Torsions- und Lateralmoden von Sensorbalken der Rasterkraftmikroskopie*. PhD Thesis, Naturwissenschaftlich-Technische Fakultät III der Universität des Saarlandes, unpublished
76. Pietrement O and Troyon M (2000) *J Colloid and Interface Science* 226:166
77. Schwarz UD (2003) *J Colloid and Interface Science* 261:99
78. Johnson KL (1985) *Contact mechanics*. Cambridge University Press, Cambridge
79. Amelio S, Goldade AV, Rabe U, Scherer V, Bushan B, Arnold W (2001) *Thin solid films* 392:75
80. Pharr GM, Oliver WC, Brotzen F (1992) *J Mat Res* 7:613

81. Vlassak JJ and Nix WD (1993) *Phil Mag* A67:1045
82. Rabe U, Amelio S, Kopycinska M, Hirsekorn S, Kempf M, Göken M, Arnold W (2002) *Surf Interface Anal* 33:65
83. Rabe U, Kopycinska M, Hirsekorn S, Muñoz Saldaña J, Schneider GA, Arnold W (2002) *J Phys D: Appl Phys* 35:2621
84. Sarioglu AF, Atalar A, Degertekin FL (2004) *Appl Phys Lett* 84:5368
85. Tsuji T and Yamanaka K (2001) *Nanotechnology* 12:301
86. Tsuji T, Irihama H, Yamanaka K (2002) *JSME Int JA* 45:561
87. Tsuji T, Irihama H, Yamanaka K (2002) *Jpn J Appl Phys* 41:832
88. Yamanaka K, Tsuji T, Irihama H, Mihara T (2003) *Proc SPIE* 5045:104
89. Wright OB and Nishiguchi N (1997) *Appl Phys Lett* 71:626
90. Dupas E (2000) *Cartographie et spectroscopie des propriétés mécaniques à l'échelle du nanomètre par spectrométrie acoustique locale à fréquence variable: Thèse no 2278, EPFL Lausanne, unpublished*
91. Wu T-S, Chang W-J, Hsu J-Ch (2004) *Microelectronic Engineering* 71:15
92. Muraoka M (2002) *JSME Int J A* 45:567
93. Muraoka M (2005) *Nanotechnology* 16:542
94. Karapetian E, Kachanov M, Kalinin SV (2005) *Phil Mag* 85:1017
95. Rabe U, Amelio S, Hirsekorn S, Arnold W (2000) in: Halliwell M and Wells NT (eds) *Acoust Img* 25. Kluwer Academic/Plenum, New York, p 253
96. Rabe U, Amelio S, Kester E, Scherer V, Hirsekorn S, Arnold W (2000) *Ultrasonics* 38:430
97. Kobayashi K, Yamada H, Matsushige K (2002) *Surf Interface Anal* 33:89
98. Yamanaka K, Maruyama Y, Tsuji T, Nakamoto K (2001) *Appl Phys Lett* 78:1939
99. Anczykowski B, Cleveland JP, Krüger D, Elings V, Fuchs H (1998) *Appl Phys A* 66:S885
100. Fukuda K, Irihama H, Tsuji T, Nakamoto K, Yamanaka K (2003) *Surf Sci* 532-535:1145
101. Hurley DC, Kos AB, Rice P (2005) *Mater Res Soc Proc* 838E:08.2.1
102. Hurley DC, Kopycinska-Müller M, Kos AB, Geiss RH (2005) *Adv Eng Mat* 7:713
103. Chang W-J, Fang T-H, Chou H-M (2003) *Phys Lett A* 312:158
104. Chang W-J (2002) *Nanotechnology* 13:510
105. Kester E, Rabe U, Presmanes L, Tailhades Ph, Arnold W (2000) *J Phys Chem Solids* 61:1275
106. Kopycinska-Müller M, Geiss RH, Rice P, Hurley DC (2005) *Mater Res Soc Proc* 838E:010.16.1
107. Prasad M, Kopycinska M, Rabe U, Arnold W (2002) *Geophys Research Lett* 29:13-1
108. Hurley DC and Turner J (2004) *J Appl Phys* 95:2403
109. Tsuji T, Ogiso H, Akedo J, Saito S, Fukuda K, Yamanaka K (2004) *Jpn J Appl Phys* 43:2907
110. Hirsekorn S, Rabe U, Arnold W (1996) *Europhysics News* 27:93
111. Hirsekorn S, Rabe U, Arnold W (1997) *Nanotechnology* 8:57
112. Muraoka M and Arnold W (2001) *JSME Int J A* 44:396
113. Turner JA (2004) *J Sound and Vibration* 275:177
114. Nayfeh AN and Mook DT (1979) *Nonlinear Oscillations*. Wiley, New York
115. Hirsekorn S, Rabe U, Arnold W (1997) *Nanotechnology* 8:57
116. Burnham NA, Kulik AJ, Gremaud G (1995) *Phys Rev Lett* 74:5092
117. Wang L (1998) *Appl Phys Lett* 73:3781
118. Sasaki N and Tsukuda M (1999) *Appl Surf Sci* 140:339
119. Lee SI, Howell SW, Raman A, Reifengerger R (2002) *Phys Rev B* 66:115409
120. Stark RW, Schitter G, Stark M, Guckenberger R, Stemmer A (2004) *Phys Rev B* 69:085412
121. Rabe U, Turner J, Arnold W (1998) *Appl Phys A* 66:S277
122. Kopycinska-Müller, M (2005) PhD-Thesis, Naturwissenschaftlich-Technische Fakultät III der Universität des Saarlandes, unpublished